Photoelectrocatalysis of paracetamol on Pd–ZnO/ N-doped carbon nanofibers electrode

Amr Nada, Benjamin Orimolade, Heba El-Maghrabi, Babatunde Koiki, M. Rivallin, Maged Bekheet, Roman Viter, Daina Damberga, Geoffroy Lesage, Igor Iatsunskyi, et al.

To cite this version:

Amr Nada, Benjamin Orimolade, Heba El-Maghrabi, Babatunde Koiki, M. Rivallin, et al.. Photoelectrocatalysis of paracetamol on Pd–ZnO/ N-doped carbon nanofibers electrode. Applied Materials Today, 2021, 24, pp.101129. 10.1016/j.apmt.2021.101129 . hal-03647328

HAL Id: hal-03647328
https://hal.umontpellier.fr/hal-03647328v1

Submitted on 17 Nov 2022

Photoelectrocatalysis of paracetamol on Pd-ZnO/ N- doped Carbon nanofibers electrode

Amr A. Nada[a,b£]; Benjamin O. Orimolade[c£]; Heba H. El-Maghrabi[a,d]; Babatunde A. Koiki[c]; Matthieu Rivallin[a]; Maged F. Bekheet[f]; Roman Viter[g]; Daina Damberga[g]; Geoffroy Lesage[a]; Igor Iatsunskyi[h]; Emerson Coy[h]; Marc Cretin[a]; Omotayo A. Arotiba[c,e]; Mikhael Bechelany[a*]

[a] Institut Européen des Membranes, IEM, UMR 5635, Univ Montpellier, CNRS, ENSCM, Montpellier, France

[b] Dept. of Analysis and Evaluation, Egyptian Petroleum Research Institute, Cairo, Nasr city P.B. 11727, Egypt.

[c] Department of Chemical Sciences, University of Johannesburg, South Africa

[d] Dept. of Refining, Egyptian Petroleum Research Institute, Cairo, Nasr city P.B. 11727, Egypt.

[e] Centre for Nanomaterials Science Research, University of Johannesburg, South Africa

[f] Fachgebiet Keramische Werkstoffe / Chair of Advanced Ceramic Materials, Institut für Werkstoffwissenschaften und -technologien, Technische Universität Berlin, Hardenbergstraße 40, 10623 Berlin, Germany

[g] Institute of Atomic Physics and Spectroscopy, University of Latvia, 19 Raina Blvd., LV 1586 Riga, Latvia

[h] NanoBioMedical Centre, Adam Mickiewicz University in Poznan, 3 Wszechnicy Piastowskiej str., 61-614, Poznan, Poland

[£] Cofirst authors

* Coresponding author: mikhael.bechelany@umontpellier.fr

Abstract

The presence of pharmaceuticals in water bodies has become a major concern in recent years. An efficient and innovative way of eliminating these pollutants is through photoelectrocatalytic (PEC) degradation owing to its environmental sustainability and its ability to remove recalcitrant pollutants. In this study, palladium loaded zinc oxide/carbon nanofibers (CZnO-Pd) were employed as a novel photoanode for PEC degradation of paracetamol. The CZnO-Pd composite was prepared through electrospinning and atomic layer deposition (ALD). The obtained materials were characterized. Photoelectrochemical studies were carried out with linear sweep voltammetry and chronoamperometry. The removal efficiency was recorded using high-performance liquid chromatography coupled to a mass spectrometer detector (HPLC-MS), while the mineralization was assessed through total organic carbon (TOC) removal. The composite electrode of CZnO-Pd nanofiber showed higher photoelectrochemical activity than ZnO carbon nanofiber, which was evident in the higher photocurrent response recorded. Upon application of the material in photoelectrocatalysis, the total removal of paracetamol was achieved within 3 h with an applied current density of 10 $mAcm^{-2}$. The percentage of TOC removal was 71.20 ± 0.31% after 4 h, which indicated significant mineralization. The results obtained in the present work reveal that Pd-ZnO/C has great potential for photoelectrocatalytic removal of organic micropollutants.

Keywords: Photoelectrocatalysis; zinc oxide; carbon nanofibers; paracetamol; water treatment

1.0 Introduction

There is a growing need for clean and safe water for industrial and domestic use. The major threat to the availability of clean water over the years is the prevalent of water pollution. Rapid urbanization and industrialization contribute largely to the rise in water pollution [1–6]. Recently, it has been identified that the complexity and the diversity of the nature of organic pollutants is a major contributing factor to the effect of water pollution. The class of water pollutants refers to as emerging contaminants that have been the focus of many research works in recent times due to the recalcitrant or persistent nature and adverse effect of these pollutants [7–10]. The most common examples of these emerging contaminants are pharmaceuticals. The contamination of water bodies by pharmaceuticals is majorly due to improper disposal of effluents from pharmaceutical industries and hospitals [11]. Additionally, effluents from households have been reported found to contain pharmaceuticals due to the improper disposal of unused or expired drugs as well as human excretion (urine) containing unmetabolized drugs [12,13]. Exposure to water contaminated with pharmaceutical residues can result in several health problems in humans depending on the nature of concentration and type of pharmaceutical as well as the duration of exposure [14]. Aquatic organisms are, however, more susceptible to hazards of pharmaceutical polluted water [15,16].

Unfortunately, traditional/conventional water treatment methods such as filtration, coagulation and adsorption have been inadequate for the complete removal of pharmaceutical pollutants from water [17,18]. This has led to the development of advanced oxidation processes (AOPs). In AOPs, complete mineralization of organics to carbon dioxide and water is achieved by the actions of *in situ* generated hydroxyl radicals (strong oxidants) [19]. Common examples of AOPs for water treatment are heterogenous photocatalysis, Fenton processes, ozonation and anodic oxidation [18,20–22]. A recent form of AOP is photoelectrochemical oxidation (PEC). In PEC, the synergistic effect of the combination of electrochemical oxidation and photocatalysis results in enhanced mineralization efficiency of the AOP [23,24]. Similar to typical photocatalysis, a semiconducting metal oxide is often used in PEC and irradiation of the semiconductor with the light of sufficient energy results to photogeneration electron-hole pairs. The holes then react with water to produce hydroxyl radicals that oxidize organic molecules. However, unlike photocatalysis, the problem of rapid recombination of photogenerated electron-hole pairs is reduced by the application of bias potential, which helps in driving the photogenerated electrons away from the semiconducting anode [23,25–27]. Additionally, PEC offers better reusability of material since the metal oxides semiconductors are used as compact and stable electrode [28]. Examples of commonly used metal oxides include TiO_2 [29,30], $BiVO_4$ [31], MoS_2 [32], Cu_2O [33], Fe_2O_3 [34] and WO_3 [35].

Zinc oxide has been widely studied for its application as photocatalyst for water treatment applications [36]. The wide use of ZnO can be rightly attributed to its fascinating properties such as ease of synthesis, non-toxicity, abundance in nature, good photocatalytic properties, large surface area, high electron mobility, remarkable thermal and chemical stability [37,38]. However, due to the large band gap of ZnO (3.37 eV), it performs better with ultraviolet light irradiation. In order to enhance its performance under visible light radiation, several strategies have been employed, such as doping with metals, metal loading, morphological control and formation of heterojunction with visible light active semiconductors [36]. ZnO nanoparticles have been employed to improve the electron-mobility in perovskite solar cells [39,40]. ZnO photoanodes have also found extensive applications in PEC water splitting [41–43]. Several interesting reported works are also available on the use of ZnO as photoanode for PEC water treatment applications. For instance, 53% removal of methylene blue dye has been recorded with the use of ZnO prepared through chemical bath deposition on silicon substrates as photoanode [44]. In another study by

Hosseini *et al.*, enhanced PEC degradation efficiency of ZnO was achieved by doping with nickel [45]. The Ni-doped ZnO achieved total removal of ciprofloxacin within 90 min with using UV light irradiation when 1.87 mA cm^{-2} current density was applied. Similarly, Feng *et al.*, reported 87.5% PEC removal tetracycline after 3 h on Ni-doped ZnO anodes with an applied potential of 0.8 V [46]. The PEC performance of Ni-doped ZnO was found to be 17% higher than the undoped. The increased performance of ZnO has also been reported in its heterostructures. For example, 100% removal of Acid Red 1 has been achieved with the use of ZnO/MoS_2 photoanode, which was higher than 53% removal recorded on pristine ZnO anode [47]. ZnO/$BiVO_4$ photoanodes have also been successfully applied for the removal of organics [48,49]. On the other hand, Carbon nanofibers (CNFs) incorporating with metal oxide nanoparticles (NPs) are interesting materials for water treatment via photo-electrocatalysis technique because of their high dimensional stability, large specific surface, good electrical conductivity, high electrocatalytic activity as well as the ability to minimize electrode surface fouling [50–52]. CNF-based electrodes are among the most interesting electrode materials for water treatment [53], electrochemical water splitting [54,55] and fuel cells [56]. In addition, the CNF has many active sites, good electrical conductivity, mechanical stability and electrolyte diffusion [57].

In this present study, palladium loaded zinc oxide/carbon nanofibers are used as suitable photoanode for the removal of paracetamol as a model pollutant. The composite materials were prepared through the combination of atomic layer deposition and electrospinning. ZnO/CNFs materials were firstly prepared through electrospinning. This is because of the advantages of electrospinning, such as being a low-cost method and the ease of controlling the size, porosity and morphology of nanofibers [58–60]. Moreover, carbon nanofibers have proven to possess attractive attributes, including high electrical conductivity and excellent mechanical stability. ALD was subsequently used to deposit palladium on the ZnO/CNFs because, with ALD, the nanoscale dimensions of nanoparticle thin films can easily be controlled [61–63]. The extent of PEC removal and mineralization of paracetamol molecules using the fabricated electrode was studied in detail using chromatographic technique and total organic carbon evaluation. From the results obtained, the prepared anode has great potential for the removal of organics from wastewater through PEC applications.

2. Experimental

2.1 Materials and chemicals

Polyacrylonitrile (PAN, Mwt ~150000, CAS 25014-41-9, Sigma-Aldrich), Zinc (II) acetate dihydrate ($Ni(OCOCH_3)_2{\cdot}2H_2O$, 99.9%, CAS No. 5970-45-6, Sigma-Aldrich), N,N-Dimethylformamide (DMF, 98%, CAS No. 68-12-2, Sigma-Aldrich) and ethanol (C_2H_5OH, 99%, CAS No. 64-17-5, Sigma-Aldrich) were used for electrospinning of CNFs decorated with ZnO NPs. Palladium (II) hexafluoroacetylacetonate ($Pd(C_5HF_6O_2)_2$, CAS 64916-48-9, 99%, Sigma-Aldrich) was used as Pd precursor and formaldehyde (HCHO, CAS No. 50-00-0, 37%, Sigma-Aldrich) used as co-reactant for ALD deposition of Pd NPs. Milli-Q water was used without further purification. Paracetamol (CAS number: 103-90-2), sodium sulphate (anhydrous, ≥99%; CAS number: 7757-82-6), absolute acetone (99%; CAS number: 67-64-1), formic acid (CAS number: 64-18-6), acetonitrile (HPLC grade; CAS number: 75-05-8), isopropanol (≥99.5%; CAS number: 67-63-0), sodium ethylenediaminetetraacetate (≥98%; CAS number: 6381-92-6) and p-benzoquinone (≥98%; CAS number: 106-51-4) were obtained from Sigma-Aldrich (Germany).

2.2 Synthesis of ZnO-Carbon Nanofibers composites

Zn@CNF was prepared by electrospinning followed by thermal preoxidation and then thermal treatment (CZnO). First, 2 g PAN powder was dissolved in 20 mL DMF under vigorous magnetic stirring until obtaining a uniform PAN precursor solution. Then, 1 g zinc acetate powder was added. The mixture solution was lifted under stirring overnight to the obtained Zn- PAN precursor solution. The electrospinning process was performed at a distance of 15 cm (solution syringe tip to collector), a voltage of 15 kV, a feeding rate of 0.5 ml/min, and a drum rotation speed of 300 rpm. The as-prepared Zn-PAN nanofibers first underwent peroxidation step at 250 °C for 2 h in an air atmosphere and then a thermal carbonation step at 800 °C for 1 h in N_2 atmosphere. The heating and cooling rates were kept constant at 1 °C/min. For comparison CNFs were prepared as the previse method without Zn precursor (CNF sample).

2.2 Deposition of Pd@ ZnO-Carbon Nanofibers composites

The ALD deposition of Pd was carried out in a low-pressure thermal (home-built) ALD reactor. A detailed description of this reactor can be found in a previous study [54]. The precursors, consisting of $Pd(hfac)_2$ and reducing agent formalin, were contained in stainless steel cylinders whose lines were heated at 70 °C and 100 °C, while the deposition chamber was pre-heated at 220 °C. The ALD cycle used for this study was consisted of 5 s pulse of $Pd(hfac)_2$, 15 s exposure, and 10 s purge, while the formalin had 1 s pulse, 15 s exposure, and 60 s purge. The ALD cycles were repeated 100 and 200 times to get CZnO-Pd100 and CZnO-Pd200, respectively.

2.3 Characterisation of materials

The crystallinity of the prepared materials was analysed using X-ray diffraction (XRD) with a PANAlytical Xpert-PRO diffractometer equipped with an Xcelerator detector and using a Ni-filtered Cu-radiation (CuKα1 radiation wavelength 0.1540598 nm and CuKα2 radiation wavelength 0.1544426 nm). Raman spectra were measured on a Senterra Bruker using a doubled Nd:YAG laser (λ= 532 nm) at a power of 10 W and an objective microscope lens of 100x. The elemental composition on the surface of the grown thin films was determined by X-ray photoelectron spectroscopy (XPS) on an Escalab 250 (Thermo Fisher Scientific, USA) using a monochromatic Al K Alpha (1486.6 eV) at 2kV and 1 µA. The morphology of nanofibers was put in evidence by using a Hitachi S4800 (Japan) scanning electron microscope (SEM). The fiber morphology was also examined using high-resolution transmission electron microscopy (HRTEM, JEOL JEM 2100, Japan) working at 200kV equipped with energy-dispersive X-ray (EDX) spectroscopy. Diffuse reflectance was measured by using HR2000+ Ocean Optics spectrometer (USA), integration sphere and Deuterium-Tungsten Halogen light source DH-2000. Photoluminescence (PL) spectra of samples were measured in the range of 350-850 nm using HR2000+ Ocean Optics spectrometer (USA). Excitation of photoluminescence was performed by Nd:YAG laser (China) (λ=266 nm, output power 29 mW).

2.4 PEC degradation experiments

The prepared materials were deposited onto FTO glass with a coverage of approximately 1 cm^2 and were used as electrodes (photoanodes). The experiments were carried out in a 100 mL capacity undivided two-electrodes cell and a power source (CNB Electronique, EU) was used to control the applied current within the cell. Platinum mesh was used as the cathode and its distance from the anode was kept constant at 3 cm. A 150 W linear halogen lamp (in the range of 420-600 nm) was used as the light source and the photoanode was irradiated from the rear with a distance of 20 cm from the lamp. The working solution consisted of 50 mL 0.1 mM paracetamol prepared in a solution of 50 mM Na_2SO_4 (supporting electrolyte). All the experiments were performed at neutral pH. Sample aliquots were taken at specified time intervals (20, 40, 60, 90, 120, 150, 180 min) for paracetamol concentration and total organic carbon contents.

2.5 Analytical Procedures

Decrease in the total organic carbon (TOC) was used to assess the extent of mineralization of the paracetamol molecules by measuring the TOC contents of the initial and aliquots solutions on a TOC-L CSH/CSN Shimadzu (Japan) analyzer. Calibration curves for total carbon (TC) and inorganic carbon (IC) analysis were built up by automatic dilution of standards solutions of TOC (potassium hydrogen phthalate) and IC (sodium hydrogen carbonate). The TOC data obtained were then used to estimate the mineralization current efficiency (MCE, %) of the solutions over a specified time t (h) using equation 1 [64].

$$\mathrm{MCE}(\%) = \frac{\mathrm{nFV_s\Delta(TOC)_{exp}}}{4.32\times10^{7}\ \mathrm{mIt}}.100 \qquad (1)$$

The number of electrons consumed in the mineralization of each paracetamol molecule is represented by n, F is the Faraday constant (96485 C mol^{-1}), V_s is the solution volume (L), $\Delta(TOC)_{exp}$ is the experimental TOC decay (mg L^{-1}), 4.32×10^7 is a conversion factor (3600 s $h^{-1}\times$12000 mg carbon mol^{-1}), m is the number of carbon atoms in each paracetamol molecule (8 atoms), the current passing through the system in time t is denoted as I. The number of electrons (n) consumed for complete mineralization was 34 for the paracetamol molecule, according to the stoichiometry of the reaction in equation 2 [65]:

$$C_8H_9NO_2 + 14H_2O \rightarrow 8CO_2 + NH_4^+ + 33H^+ + 34e^- \qquad (2)$$

The concentration decay of paracetamol molecules was estimated through high performance liquid chromatography – mass spectrometry (HPLC-MS). HPLC-MS was carried out with a Waters 2695 pump, an auto sampler with 20 µL loop, a Waters 2695 separation module (HPLC), and a Waters Micromass (Wythenshawe, Manchester, UK) Quattro Micro mass spectrometer equipped with ESI (Electrospray Ionization). HPLC was performed on a Waters – Xselect HSS T3 column at a column temperature of 25 °C. The mobile phase was a Buffer A (HPLC grade water + 0.1% formic acid) and Buffer B (HPLC grade acetonitrile + 0.05% formic acid). The flow-rate was constant at 0.25 mL min^{-1}, with a split of 20% to the mass spectrometer. The triple quadrupole MS was operated in selected-ion-recording (SIR) mode with compounds being ionized in the negative electrospray ionization mode. To achieve the best sensitivity, the MS was adjusted to facilitate the ionization process. The detection conditions were: capillary potential 3.5 kV, cone potential 30 V, source temperature 120 °C, desolvatation temperature 450 °C, cone gas flow 50 L h^{-1}, and desolvatation gas flow 450 L h^{-1}. Nitrogen (99.5% purity) was the nebulizer gas.

Results and discussion

3.1 Characterisation results

The CNF and CZnO were elaborated via electrospinning of polymeric solution containing PAN and zinc acetate as precursors, followed by pyrolysis under nitrogen at 800 °C for 1 h in N_2. CZnO-Pd100 and CZnO-Pd200 samples were prepared on CZnO as a substrate by the deposition of metallic Pd by ALD using 100 and 200 cycles, respectively. As shown in Figure 1a, two broad reflections, which correspond to the (002) and (101) reflections of a turbostratic structure of carbon

[66], are observed in the XRD pattern of CNF sample. The crystallite size of the turbostratic carbon along the c-axis (L_c) in CNF is found to be 0.8 nm, as revealed by Rietveld refinement of XRD data. Moreover, the average number of graphite stacking layers (N_c), which is estimated from the interlayer spacing d_{002} and crystallite size along the c-axis (L_c) [67], is found to be 2.5. The intensities of these XRD reflections in the XRD pattern of CZnO are varnished, indicating that the structure of carbon becomes highly disordered by introducing ZnO to the surface of the nanofibers. Moreover, no XRD reflections corresponding to any of crystalline Zn or ZnO are observed in the XRD pattern of CZnO, CZnO-Pd100 and CZnO-Pd200 samples, which can be explained by the amorphous structure or small weight fractions of ZnO in these samples in order to be detected by XRD measurements. However, XPS analysis (Table S1) shows that the CZnO sample contains a high amount of elemental Zn (6.7 wt%, which corresponds to 8.3 wt% of ZnO) on the surface of carbon nanofibers, suggesting the amorphous structure of ZnO in the sample. In contrast, Pd crystallized in metallic form in CZnO-Pd100 and CZnO-Pd200 samples during ALD deposition. All the peaks appearing on the XRD patterns can be indexed to the cubic structure of metallic Pd (PDF No. #00-065-6174). A similar crystallite size of 3.7 nm is determined by Reitveld refinement for metallic Pd in both samples, which suggests that the increase in the deposition time might increase the number of deposited Pd particles on the surface of carbon nanofibers, but without altering their crystallinity.

The incorporation and structure of ZnO and Pd on the surface of carbon nanofibers were further investigated by Raman spectroscopy (Figure 1-b). All the prepared nanofibers displayed the fingerprint bands of carbon, such as the disorder peak (D-band) at 1354 cm^{-1} and graphite peak (G-band) at 1591 cm^{-1}. The presence of D band, which is characteristic of the disordered sp^2-hybridized modes in the rings, confirms the turbostatic structure of carbon in the samples as revealed by XRD. In contrast, the G-band corresponds to the vibrational stretching mode of in-plane sp2 -hybridized C atoms [68]. The relative intensities (R = I_D/I_G value) of D and G bands could be used to evaluate the degree of structurally ordered graphite crystallites in carbon materials.[53] The *R* value of CNF was 0.93, and it increased to 1.18, 1.14 and 1.15 for CZnO, CZnO-Pd100 and CZnO-Pd200, respectively, indicating the increase in the degree of disordered carbon structures with introducing ZnO into the carbon nanofibers, which is in good agreement with XRD results. Moreover, no Raman modes were observed for ZnO in the spectra of CZnO, CZnO-Pd100 and CZnO-Pd200 samples, confirming the amorphous structure of ZnO as revealed by XRD analysis. In addition, strong bands are detected at 633 and 629 cm^{-1} in the Raman spectra of CZnO-Pd100 and CZnO-Pd200, respectively, which can be attributed to the active B_{1g} vibration modes of PdO [69]. The presence of PdO in the CZnO-Pd100 sample is also confirmed by XPS characterization, as discussed below.

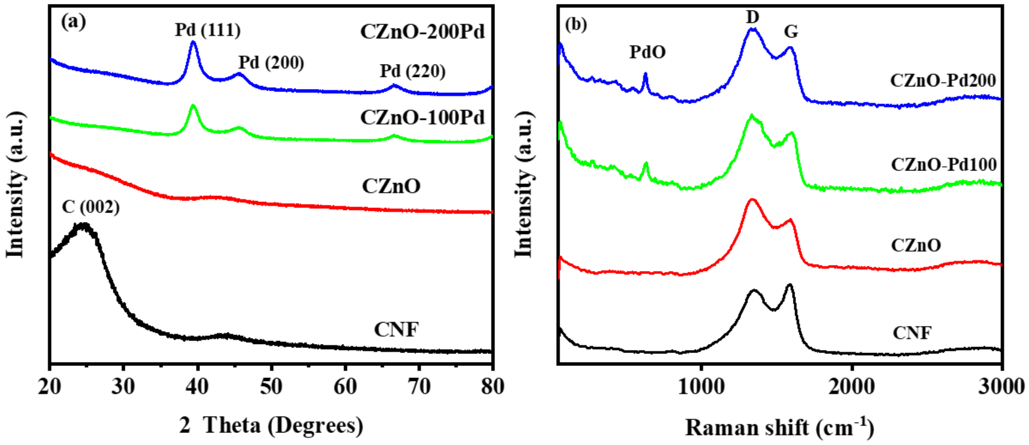

Figure 1: (a) XRD patterns of prepared CNF, CZnO, CZnO-Pd100, CZnO-Pd200 nanofibers. (b) Raman spectra of prepared nanofibers.

The elemental compositions as well as the coordination and the oxidation states of different elements in the obtained samples were characterized by XPS measurements. As shown in Figure S1 and Table S1, the survey XPS spectra confirm the successful incorporation of elemental Zn and Pd at the surface of the carbon nanofibers. The mass fraction of elemental Zn on the surface of CZnO sample is found to be 6.7 wt% and decreased to 4.1 wt% on the surface of CZnO-Pd100 due to the successful deposition of Pd (i.e., 33 wt% of the sample). Additionally, remarkable amounts of nitrogen are detected in all the samples, suggesting the nitrogen doping of the carbon nanofibers. The N-doping of carbon nanofibers can be explained by the high content of N in PAN polymer and the pyrolysis of the polymeric precursors under N_2 atmosphere. As shown in Table S1, the mass fraction of N in CZnO sample is four times higher than that in the CNF samples, which indicates that zinc salt might stabilize the nitrile group in the polymer during the electrospinning process, and thus, it enhanced the N-doping of carbon nanofibers. The high-resolution XPS spectra of C 1s, O 1s, N 1s, Zn 2p, and Pd 3d orbitals are shown in Figure 2 a-e. The spectrum of C 1s (Figure 2-a) could be deconvoluted into four peaks located at about 284.6, 285.6, 287 and 289 eV, corresponding to sp^2 hybridized graphitic carbon C-C bond, C-N bond, C-O bond, and C=O bond, respectively [70]. As shown in Figure 2-b, O 1s spectrum of CNF sample can be fitted with two peaks at 532.2 and 534 eV, which can be attributed to C=O and C-O bond, respectively. An additional peak is observed at about 530.5 eV in the O 1s spectra of CZnO and CZnO-Pd100 samples, which can be assigned to the lattice oxygen of ZnO. As displayed in Figure 2c, the N 1s spectra can be fitted with three peaks a ~ 398, 399.4 and 400.9 eV, which can be assigned to pyridinic N, pyrrolic N and graphitic N, respectively. The pyridinic N and pyrrolic N species become the dominant nitrogen species in CZnO and CZnO-Pd100 samples, suggesting the improvement of the electrochemical performance of these samples [70]. The incorporation of ZnO in CZnO and CZnO-Pd100 samples is further confirmed by detecting the peak at 1022 eV corresponding to Zn 2p3/2 in ZnO (Figure 2d) [71]. The Pd 3d spectrum of In CZnO-Pd100 nanofiber (Figure 2-e) can be deconvoluted into two peaks at ~ 335.6 and 337 eV, corresponding to Pd^0 and Pd^{+2} species, respectively. The Pd^{+2}/Pd^0 ratio is found to be 0.15, suggesting the small mass fraction of oxidized Pd^{+2} species in the samples, which agrees with the results of Raman characterizations.

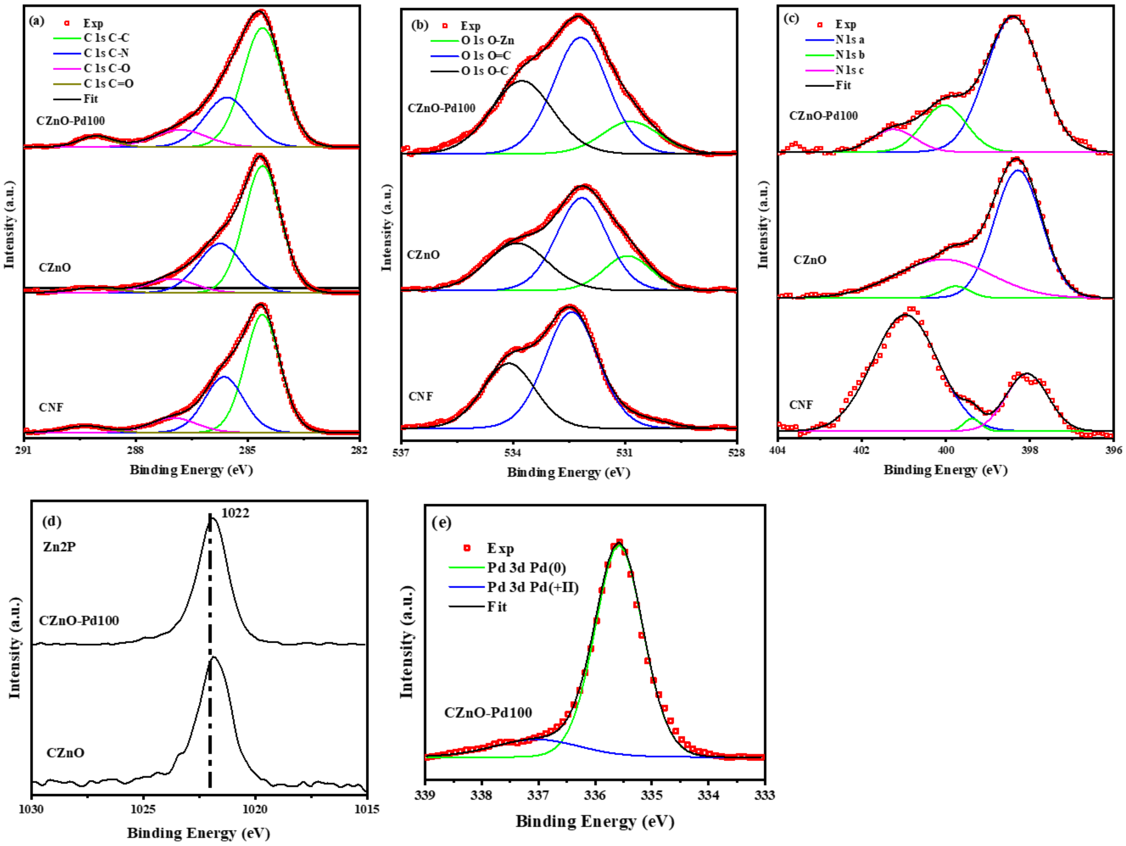

Figure 2: (a) High-resolution XPS spectra of C 1s (a), O 1s (b), N 1s (c), Zn 2p (d), and Pd 3d (e) for CNF, CZnO and CZnO-Pd100.

The morphology of the elaborated nanofibers was investigated by SEM characterization, as illustrated in Fig. 2(a-h). The CZnO, CZnO-Pd100 and CZnO-Pd200 samples consist of carbon fibers with an average diameter of 0.25 ± 0.02 µm, which is smaller than that of CNF sample (0.45 ± 0.02 µm). This result suggests that the addition of zinc salt during the electrospinning process hinders the growth of the carbon nanofibers during the pyrolysis. As shown in Figure 3e-h, the metallic Pd are uniformly deposited as spherical particles with an average diameter of 5.6±1nm on the surface of the carbon nanofibers in the CZnO-Pd100 and CZnO-Pd200 samples. Although the particle size of metallic Pd does not change with increasing the deposition time, the number of metallic Pd increases, which agrees with XRD results. The homogeneous distribution of Zn on the entire surface of carbon nanofibers is confirmed by TEM, STEM, and EDX mapping, as presented in Figure S2. In contrast, the metallic Pd nanoparticles are deposited on the edge/shell of the nanofibers to form coaxial or core/shell structure, as revealed by HRTEM (Figure 3i-l) and EDX mapping (Figure 3m-o). The fast Fourier transform (FFT) pattern of CZnO-Pd100 nanofibers for a square box (inset Fig. 3l) confirmed the cubic structure of metallic Pd nanoparticles by detecting the d spacing 0.23 nm corresponding to the (111) planes of metallic Pd.

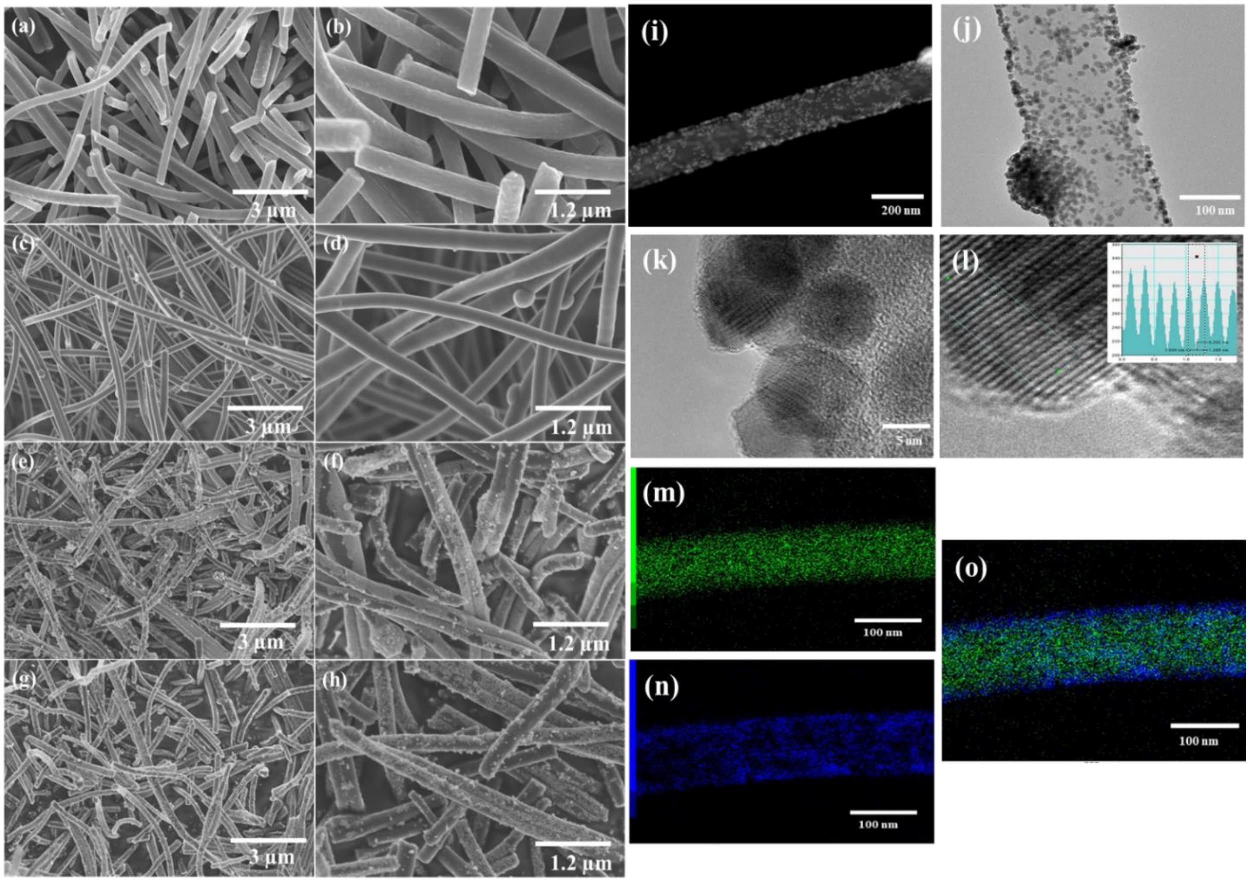

Figure 3: Field emission SEM images of the prepared nanofibers; CNF (a,b), CZnO (c,d), CZnO-Pd100 (e,f), and CZnO-Pd200 (g,h). High-resolution transition microscope of CZnO-Pd100 (i - l) and the fast Fourier transform (FFT) pattern of the area marked by the blue square box of CZnO-Pd100 and the corresponding intensity profiles in inset (l), with EDX elemental mapping of CZnO-Pd100 the zinc (m), palladium (n) and Zn overlap Pd (o).

In the next step, the optical properties influence of Pd on CZnO nanofibers were detected by the optical band gap by UV-vis. in addition, the generation and stability of e^-/h^+ were detected by PL side by side of determine the optical band gap. The measured reflectance spectra were converted into absorption spectra according to equation 1 [72].

$$F = \frac{(1-R)^2}{2 \cdot R} \text{ (*)} \qquad \text{equation 1}$$

where the parameters F and R refer to the absorption coefficient and diffuse reflectance of the sample, respectively. The obtained spectra are shown in Figure 4a. All samples show low absorbance in the UV range and high absorbance in the visible range. Although no absorption edge is observed for ZnO-based samples, absorbance value is increased in the visible range by adding ZnO and Pd on the surface of carbon nanofibers. This finding will be explained further.

PL spectra of the samples are shown in Figure 4b. Weak characteristic PL peak is observed at 3.25 eV in the spectrum of CNF sample, which could be related to delocalized π electrons available at the surface of carbon nanofibers [73]. The successful addition of ZnO on the surface of carbon nanofibers is confirmed by the strong PL peak at 3.24 eV observed in the spectrum of CZnO sample that corresponds to ZnO excitonic emission [72]. The deposition of metallic Pd on the surface of ZnO/CNF had different effects on ZnO emission: enhancement of ZnO emission in ZnO-PD100 samples and quenching for ZnO-PD200 samples. According to the literature [74–78], Pd nanostructures have at least 2 absorption bands: in UV and visible ranges, related to localized surface plasmon resonance (SPR) effect [74–78]. The position and FWHM of the bands depend on the size and shape of Pd nanostructures [79]. It was shown that due to differences between ZnO and Pd work functions, Schottky barrier is expected at ZnO/Pd interface, inducing electron flow from conduction band (CB) of ZnO to Pd [79,80]. It results in increase of absorption and decrease of ZnO emission. However, alternative mechanisms at ZnO/Pd interface are possible [69,71]. It was reported that UV emission of ZnO can be increase due to passivation of surface states during Pd deposition [79,81]. We suppose, that Pd morphology will define the ZnO/Pd optical properties. Comparative analysis of absorption and photoluminescence spectra points to the fact, that the absence of characteristic absorption edges of ZnO in ZnO/Pd nanostructures points to hot electron effect (HEE) in Pd nanoparticles [82]. This is effect is based on transition of excited SPR electrons from Pd to CB of ZnO [82]. The hot electron effect is assisted with increase of visible absorption and fading of UV absorption bands [82]. The HEE depends on morphology of ZnO/Pd interface. At lower Pd concentrations, Pd layer is cluster-like and increase of PL can be observed. The increase of Pd thickness might promote light scattering (no excitation light in absorbed by ZnO) and, thus, diminishing ZnO emission.

Moreover, the increase in the absorbance of carbon-based samples (Figure 4a) points to a wide absorbance band of Pd nanostructures in the range of 1.5-3 eV. The absorption values increase with increasing the amount of Pd on the surface of carbon nanofibers. Forming of carbon-ZnO and Pd/ZnO interfaces makes impact on photoluminescence properties of the composite nanomaterial [81,83–85]. The presence of carbon nanofibers with ZnO results in quenching of photoluminescence due to charge transfer [83]. Deposition of Pd layer over ZnO could result in quenching of visible PL [81,84] and/or quenching of PL in all measured spectra due to the passivation of ZnO photoluminescence centers [85]. The common effect in Pd/ZnO nanostructures was observed in blue shift of UV PL peak [81,84,85]. In the present work, no shift of PL was observed for ZnO/Pd100 samples. The increase of Pd concentration resulted in almost complete quenching of the PL. However, the UV peak in CZnO/Pd sample was similar to the PL peak in untreated CNF.

It was shown that UV emission in carbon nanomaterials corresponds to π- π transition in C=O bonds [86,87]. The observed emission could be explained from oxidized surface of CNF in case of full passivation of ZnO emission centers.

In addition, the valence band (VB) XPS was studied for the extra analysis of electronic states induced by defects above the valence band as presented in Figure 4c-d. It is clearly seen few XPS features at 2.5 eV, 5 eV and 10 eV attributed to Pd 4d, O 2p and Zn 3p peaks, respectively. Typically, the density of states of ZnO below Fermi level is consisted from two bands: the upper peak at ~10 eV mainly derived from Zn 3d orbitals, and the lower band at ~5 eV arises from almost O 2p hybridized with the Zn 4s and Zn 4p states [88]. We estimated the VB maximum (VBM) using standard method as described elsewhere [89]. The VB spectrum for the CNF is in a good agreement with those reported for carbon [90]. The VBM of Pd (estimated from the extrapolation) was observed at around 2 eV above the Fermi level (EF) indicating the metallic behavior, while the VBM for CZnO had a value around 1.9 eV below the EF. Typically, the values of VBM for undoped crystalline ZnO are in the range of 2.54 eV to 2.11 eV. This shift of the VBM might be associated with an increase in the concentration of defects and/or doping (carbon, nitrogen etc.) of ZnO. Besides, we may observe the shift of Zn 3p maxima from 10.19 eV to 10.42 eV after the Pd deposition. This can be explained by the redistribution of electron density in the d-orbitals of the Zn^{2+} and the Pd^{2+} which is believed to have produced additional energy levels near the VB of the ZnO narrowing its band gap, what as a consequence may change photocatalytic properties of produced nanocomposites [89].

Hydrogen Evolution Reaction (HER) of the prepared nanofibers has been studied to manifest the role of palladium. The HER linear sweep voltammetry curves (LSV) of the prepared nanofibers were presented in Figure 4e. From the data, the CZnO-Pd100 has better electrochemical activity than other prepared nanofibers. It was shown lower overpotential than other nanofibers (250 mV) at 10 mA/cm^2 of the current density. In contrast, the overpotential of CNF, CZnO and CZnO-Pd200 are 695, 620 and 441 mV at 10 mA/cm^2 of the current density, respectively. CZnO-Pd100 recorded the best activity of HER due to the good distribution of Pd NPs on the nanofibers. We note here that the CZnO-Pd200 has less activity than CZnO-Pd100 because of the Pd NPs aggregation on the surface of the nanofibers as reported elsewhere [52,54,91]. Furthermore, the electrochemical impedance has been measured as illustrated in Figure 4f. The charge transfers resistance (Rct) was calculated from the Nyquist plots in Figure 4f. The CZnO-Pd100 recorded lower resistance (80 Ω) than the other nanofibers CNF (275 Ω), CZnO (240 Ω) and CZnO-Pd200 (120 Ω), in agreement with its HER activity results and lower overpotential.

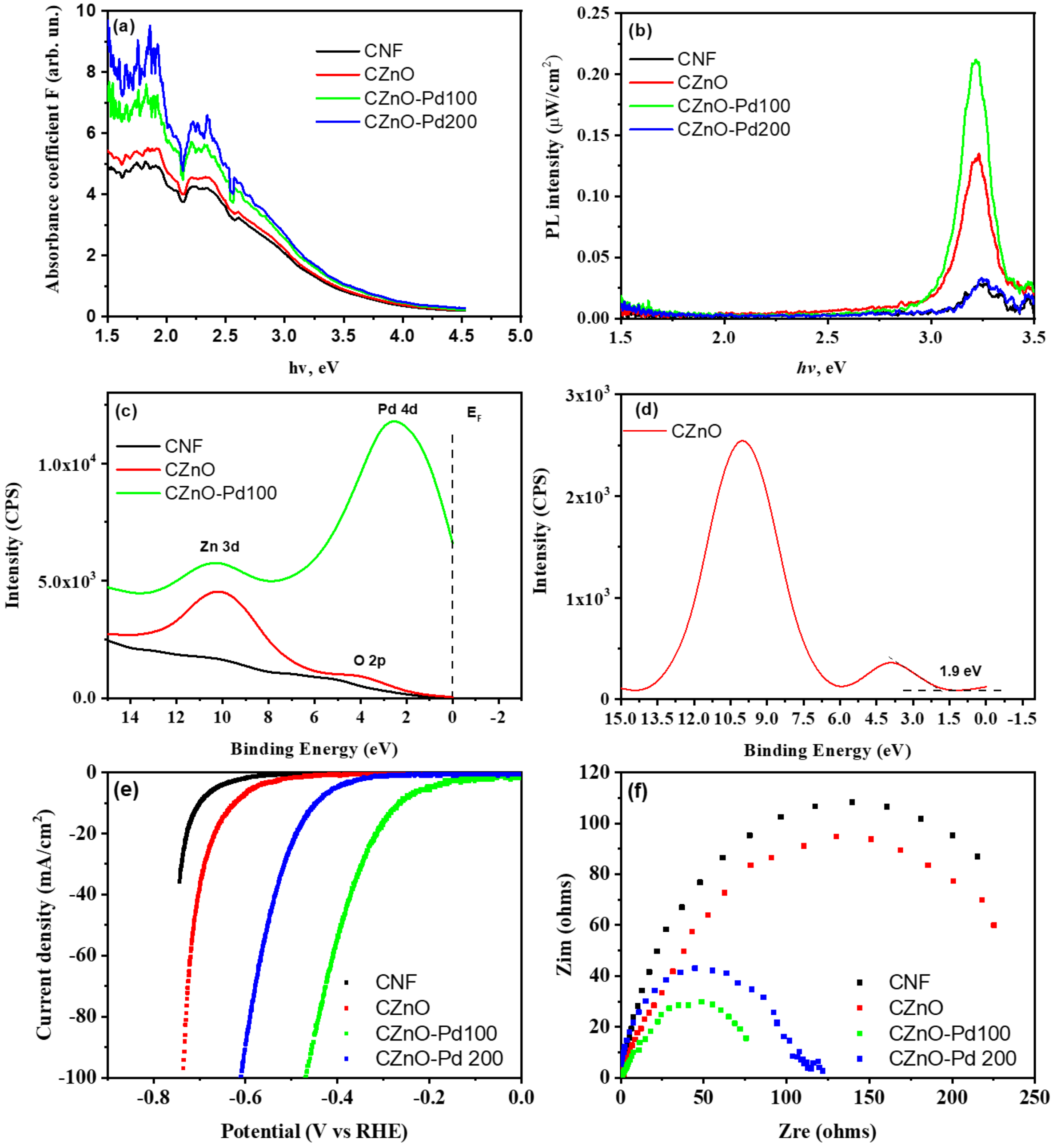

Figure 4: Absorbance spectra of CNF, CZnO, CZnO-Pd100 and CZnO-Pd200 nanofibers (a); PL of CNF, CZnO, CZnO-Pd100 and CZnO-Pd200 nanofibers (b); VB-XPS of CNF, CZnO, CZnO-Pd100 (c); Zooming of VB-XPS of CZnO (d); HER of CNF, CZnO, CZnO-Pd100 and CZnO-Pd200 nanofibers (e); and EIS of CNF, CZnO, CZnO-Pd100 and CZnO-Pd200 nanofibers (f).

3.2 PEC degradation of paracetamol

The results for the PEC degradation of paracetamol using the prepared photoanode are presented in Figures 5a-d. After 150 min, total removal (100%) of paracetamol was achieved using CZnO-Pd100 anode (Fig 5a) with an applied current of 10 mA cm^{-2} (corresponding to 4.2 V). The incorporation of Pd on the surface of ZnO/CNFs led to this impressive result because the CZnO anode achieved just 56.40 ± 2.10% PEC removal of paracetamol after 150 min. This could be due to the fact that transition metals improve the photocatalytic efficiencies of semiconductors by increasing their light absorptivity and limiting spontaneous recombination. This is in line with previous studies where doping ZnO with Pd has also been reported to increase the photocatalytic efficiency of ZnO [92,93]. However, with CZnO-Pd200 photoanode, the percentage removal was about 80.00 ± 0.20% after 150 min, and this revealed that the excessive amount of Pd in the composite material could diminish its efficiency. The CZnO-Pd100 photoanode was subsequently used to access the degradation of paracetamol through an electrochemical oxidation and photocatalytic process in order to establish the superiority of PEC process. As shown in Figure 5b, in the absence of light, the percentage removal of paracetamol decreased to about 82.20 ± 0.14 % after 3 h, and this revealed that irradiation greatly enhanced the efficiency of the electrode. On the other hand, when the degradation experiment was performed without applying an external current (photocatalysis), the percentage removal reduced drastically to 14.30 ± 0.12%. The lower efficiency of the electrode in photocatalysis further showed that the applied current in the PEC process remarkably improve the performance of the electrode by promoting efficient charge separation since it provides a driving force for the photogenerated electron to move away from the anode surface. Additionally, anodic oxidation of the paracetamol was also possible with the application of external current.

In order to confirm the dependence of the PEC degradation process on the applied current, the experiments were also performed with the application of 5 mA cm^{-2} (3.3 V) and compared with the results obtained with 10 mA cm^{-2}. As presented in Figure 5c, at lower applied current (5 mA cm^{-2}), the percentage of paracetamol degradation was reduced to 78.11 ± 0.20% after 150 min. This clearly showed that the magnitude of applied current also has an effect on the separation of photogenerated electron-hole pairs within ZnO. The space charge region and Helmholtz layer on the surface of the photoanode largely determine the mobility of photogenerated charge carriers. Applied current increases the width of the charge region, and when this happens, the spontaneous recombination of photogenerated carriers is reduced [45]. An increase in the magnitude of applied current could increase the width of the space charge region, and this evidently led to an increase in percentage removal of paracetamol when the current was increased from 5 mA cm^{-2} to 10 mA cm^{-2}. However, too high applied current promotes oxygen generation, which decreases PEC degradation performance and could also affect the integrity of the electrode.

Kinetics study was also performed by fitting the experimental data into the pseudo second order reaction kinetics model. The apparent rate constants were obtained from the slope of the plots of $\ln C_o/C_t$ versus time (Figure 5d). In the PEC degradation processes using different photoanodes, the apparent rate constants were 7.88 x 10^{-4} min^{-1}, 6.94 x 10^{-3} min^{-1} and 9.10 x 10^{-3} min^{-1} for CZnO, CZnO-Pd200 and CZnO-Pd100 respectively. The highest rate constant obtained using CZnO-Pd100 revealed that the PEC degradation is fastest using this electrode in addition to the highest percentage removal obtained. Furthermore, the kinetics of photocatalytic, electrochemical (EC) and PEC degradation were also studied using the CZnO-Pd100 electrode. It was found that the order of increasing apparent rate constant was photocatalytic < electrochemical < PEC degradation and this also showed that a combination of photocatalysis and electrochemical degradation in the PEC process facilitated the fast rate at which paracetamol molecules were degraded. To further justify the improved performance obtained through the incorporation of visible light irradiation (photocatalysis) with applied external electric current, the degree of electrochemical enhancement (E) and the degree of process synergy (S) were obtained using equations 3 and 4 respectively [94].

$$E = (K_{PEC} - K_{PC})/K_{PEC} \tag{3}$$

$$S = (K_{PEC} - (K_{PC} + K_{EC}))/K_{PEC} \tag{4}$$

Where K_{PC}, K_{EC}, and K_{PEC} are apparent rate constants for photocatalytic (7.883 x 10^{-4} min^{-1}), electrochemical (5.37 x 10^{-3} min^{-1}) and PEC degradation (9.710 x 10^{-3} min^{-1}) of paracetamol, respectively. The degree of electrochemical enhancement was calculated to be 0.91 (91%), which established that the application of electric current has a tremendous impact on the PEC process, and the percentage removal obtained with electrochemical degradation likewise justify this. In line with this, the degree of process synergy calculated (0.323) was obviously greater than zero, which confirmed that the improved performance obtained with PEC degradation is more than the summation of the individual electrochemical and photocatalytic degradation process, revealing that the introduction of applied electric current with photocatalysis result in a synergistic effect and not cumulative/summation effect [94,95].

The catalytic performance of ZnO/Pd depends on ratio between Pd thickness and concentration of active sites at ZnO/Pd interface [82]. It was shown that catalytic performance as a function of Pd concentration had maximum between 0% Pd and 18% Pd loading. Higher concentration of Pd restricts the role of metal oxide component in photocatalysis and therefore reduces total photocatalytic effectiveness. This was in agreement with the results obtained from the PL spectra discussed earlier where increase in Pd loading resulted in light scattering effect on the surface of the catalyst, thereby diminishing its photocatalytic activity.

In the present work, ZnO-Pd100 samples showed higher performance compared to ZnO-Pd200 due to higher concentration of active sites. This was confirmed by optical characterizations (photoluminescence) where, we can get highly efficiency at the certain amount of Pd active sites (CZnO-Pd100).

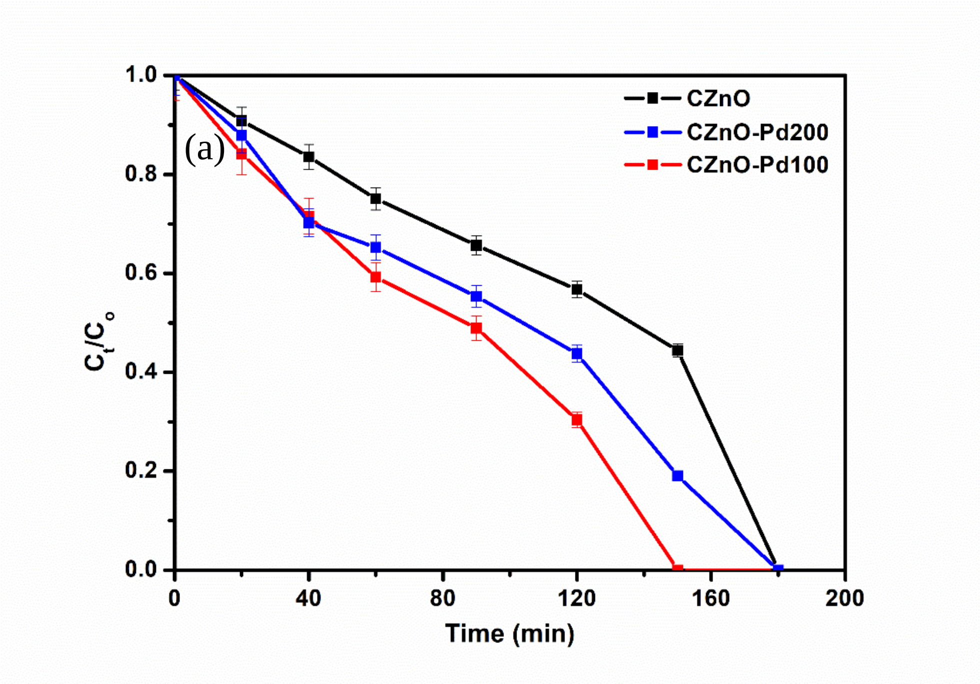

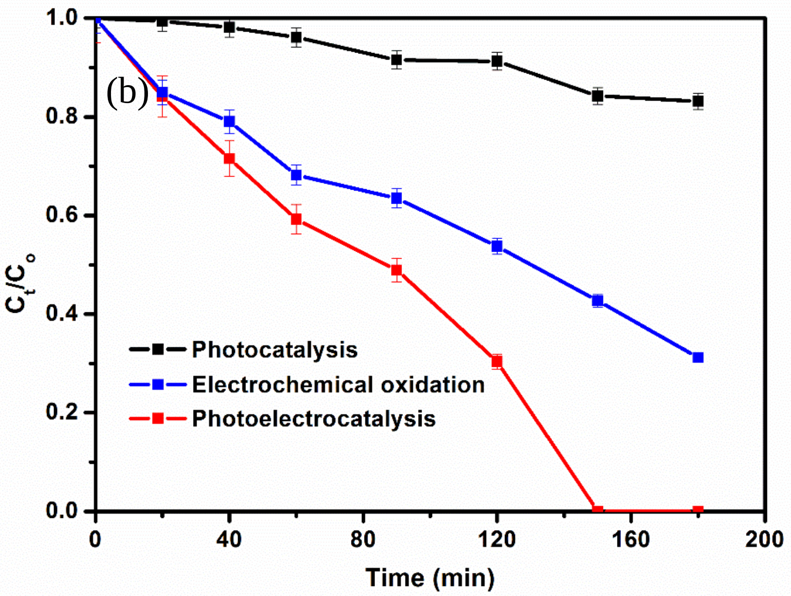
(b)
1.0
0.8
0.6
0.4
0.2
0.0
C_t/C_o
0
40
80
120
160
200
Time (min)
Photocatalysis
Electrochemical oxidation
Photoelectrocatalysis

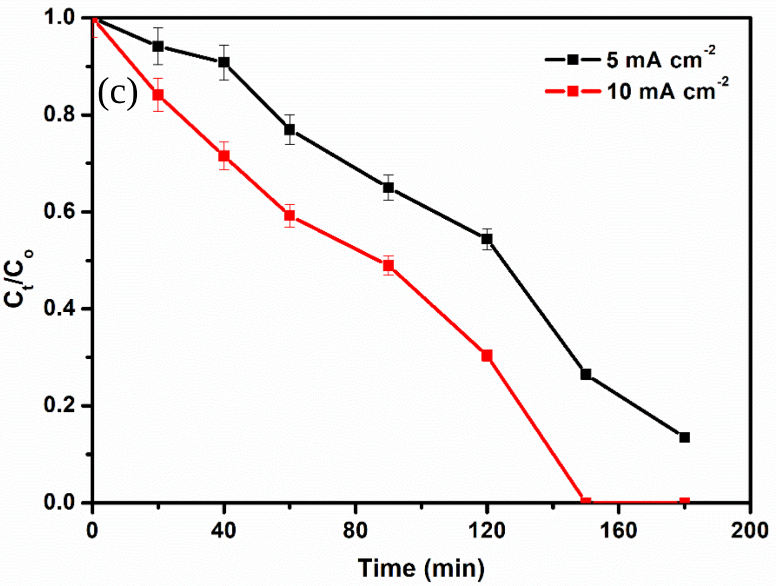
(c)
1.0
0.8
0.6
0.4
0.2
0.0
C_t/C_o
0
40
80
120
160
200
Time (min)
5 mA cm^{-2}
10 mA cm^{-2}

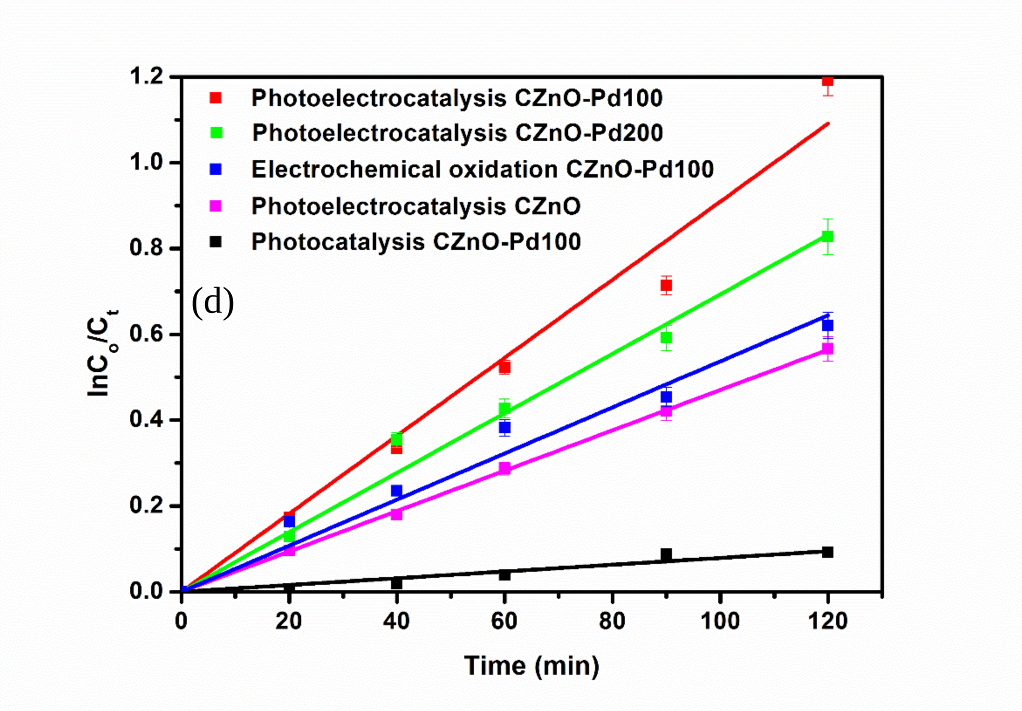

Figure 5: Normalized concentration decay versus time plot for PEC degradation of paracetamol using (a) CZnO, CZnO-Pd100 and CZnO-Pd200; (b) Photocatalysis, electrochemical oxidation and photoelectrocatalysis using CZnO-Pd100; (c) Photoelectrocatalysis at different current densities using CZnO-Pd100; (d) Corresponding kinetics plot for the processes at 10 mAcm^{-2} (0.1 mM paracetamol; pH 7; 50 mM Na_2SO_4)

3.2.1 TOC removal and reusability of the electrode

In PEC degradation of organics, similar to other advanced oxidation processes, it is envisaged that the total mineralization of organics to water and carbon dioxide would occur after some period of reaction. In order to quantify the extent of mineralization of paracetamol using the composite electrode of CZnO-Pd100, the total organic carbon (TOC) content was measured as the PEC process progressed. As shown in Figure 6a, the percentage of TOC removal was approximately

71.20 ± 0.31% after 4 h. This clearly revealed that significant mineralization of paracetamol molecules occurred in the PEC degradation. From the TOC results obtained, it became obvious that the paracetamol was broken down totally to other smaller organics first, and this accounted for the total removal of paracetamol achieved within 150 min. Since complete removal of TOC was not recorded, smaller chain aliphatic organic acids such as fumaric, oxalic, acetic and maleic acids, which are by products of paracetamol degradation, were still present in the solution [96,97]. Additionally, the corresponding calculated mineralization current efficiency (MCE%) was found to decrease progressively with time from 15.10 ± 0.23% at 1 h to about 6.34 ± 0.03% after 4 h (Figure 6b). This suggests a gradual reduction in the oxidation ability of the process, which could be due to the generation of highly resistant short-chain hydrocarbon as by-products [98]. The reduction in the organic content over a prolonged period could also limit the mass transport as well as facilitating counterproductive reactions such as dimerization of hydroxyl radicals [99].

A desirable attribute of a potential photoanode for industrial water treatment applications is ease of reusability. The reusability and stability of the CZnO-Pd100 anode were accessed by using the electrode consecutively for eight times (8 runs or cycles) and recording the percentage removal after 2 h (Figure 6c). After each run, the electrode was simply rinsed with deionized water and air-dried overnight, unlike in some water treatment techniques where the recovery of the material is often tedious and involves the use of strong chemicals [82,83]. After the eighth run, the difference in the percentage removal was less than 4%, which confirmed the reusability of the anode. In addition, we can note also that the crystallinity and the electronic state of CZnO-Pd100 nanofibers (Figure S3) did not change after photoelectrocatalytic reaction as confirmed by XRD and XPS.

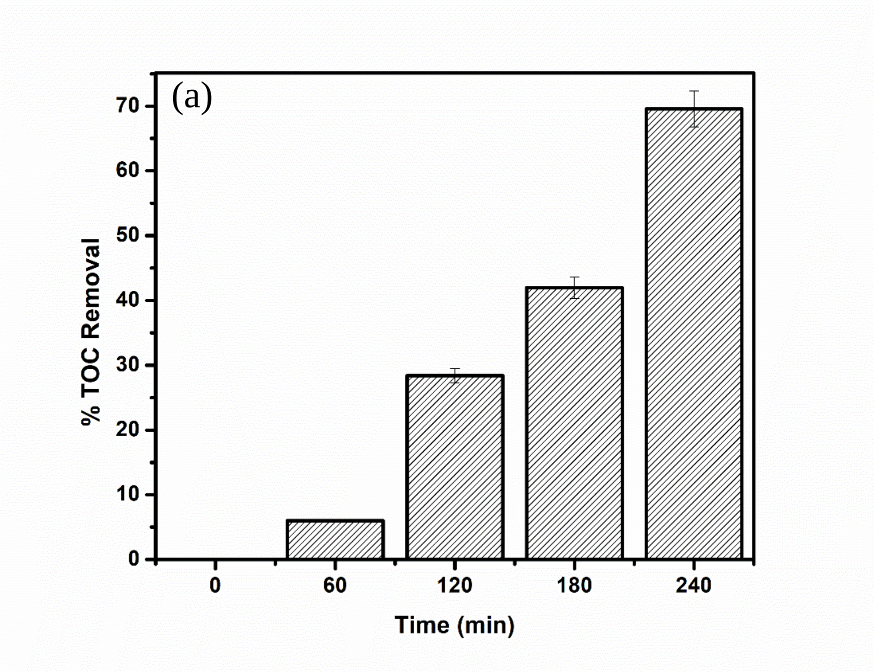
(a)
% TOC Removal
0
10
20
30
40
50
60
70
Time (min)
0
60
120
180
240

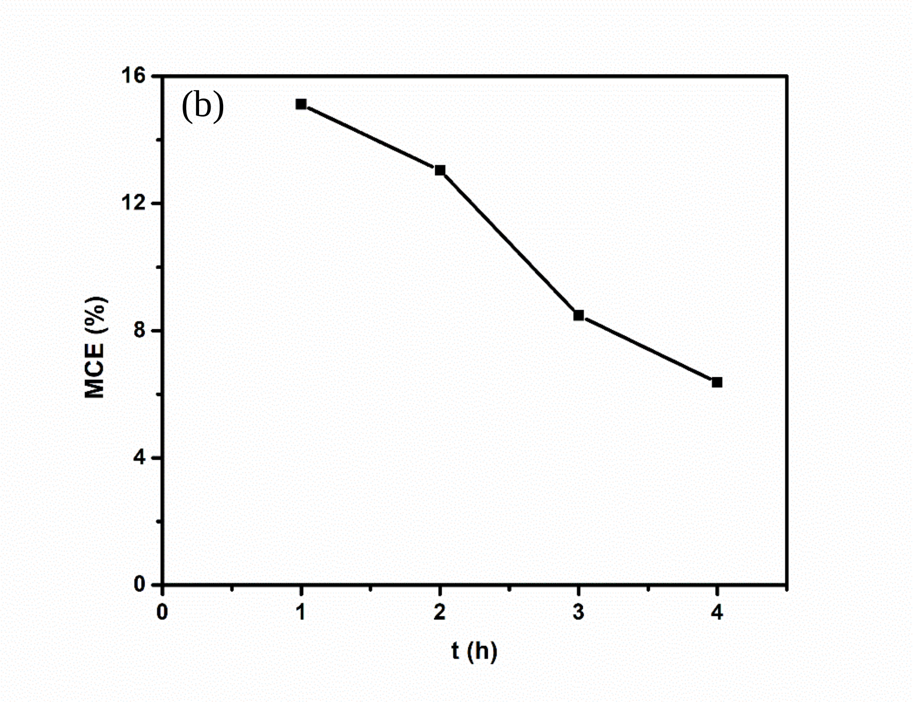
(b)
MCE (%)
0
4
8
12
16
t (h)
0
1
2
3
4

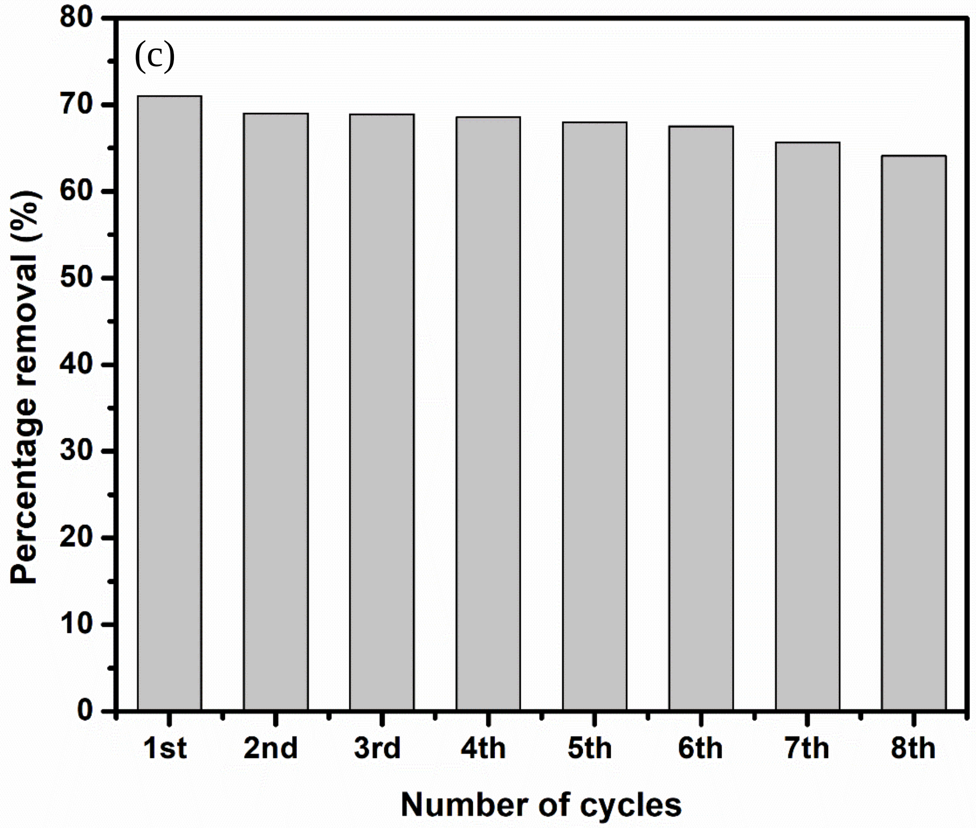

Figure 6: (a) Percentage total organic carbon removal in the PEC degradation of paracetamol; (b) Corresponding percentage mineralization current efficiency with time; (c) Reusability tests (0.1 mM paracetamol; pH 7; CZnO-Pd100; 10 mA cm^{-2})

3.2.2 Scavenger studies and proposed degradation mechanism

In a typical PEC degradation process, in addition to hydroxyl radicals, other reactive species such as photogenerated holes and superoxide radicals also contribute at different degrees to the mineralization of organic molecules [98]. The stepwise formations of these reactive species and their reaction with paracetamol molecules are presented in equations 5 – 10:

$$\mathrm{hv} + \mathrm{CZnO/Pd} \rightarrow \mathrm{CZnO/Pd}\ (\mathrm{h}^{+} + \mathrm{e}^{-}) \qquad (5)$$

$$\mathrm{e}^{-} + \mathrm{O_2} \rightarrow\ ^{\bullet}\mathrm{O_2^{-}} \qquad (6)$$

$$\mathrm{h}^{+} + \mathrm{H_2O} \rightarrow\ ^{\bullet}\mathrm{OH} + \mathrm{H}^{+} \qquad (7)$$

$$^{\bullet}\mathrm{OH} + \mathrm{paracetamol} \rightarrow \mathrm{CO_2} + \mathrm{H_2O} + \mathrm{intermediate\ products} \qquad (8)$$

$$^{\bullet}\mathrm{O_2^{-}} + \mathrm{paracetamol} \rightarrow \mathrm{CO_2} + \mathrm{H_2O} + intermediate\ products \qquad (9)$$

$$\mathrm{h}^{+} + \mathrm{paracetamol} \rightarrow \mathrm{CO_2} + \mathrm{H_2O} + intermediate\ products \qquad (10)$$

Trapping experiments were therefore conducted to understand the specific roles of hydroxyl radicals, photogenerated holes and superoxide radicals in the PEC degradation of paracetamol by the addition of 0.001 M Isopropanol (IPA), 0.02 M p-benzoquinone (p-BQ) and 0.01 M ethylenediaminetetraacetate (EDTA) to the electrolytic solution to suppress the effect of hydroxyl radicals, superoxide radicals and holes respectively [98,99]. As presented in Figure 7, upon the addition of EDTA, the percentage removal of paracetamol dropped significantly to 18.70 ± 0.20% after 2 h. This revealed that separated photogenerated holes played a major role in the mineralization of paracetamol. This is in agreement with literatures that photogenerated holes can directly oxidize organics in solution rather than generating hydroxyl radicals first in PEC systems [23]. Additionally, hydroxyl radicals also contributed to the total percentage removal obtained because when the reaction was done in the presence of isopropanol, the percentage removal was 35.10 ± 1.40%. On the other hand, in the presence of p-BQ, substantial degradation percentage was still recorded which clearly revealed that superoxide radicals played a far less role in the degradation process. With these findings, it can be established that the degradation of paracetamol molecules using the CZnO-Pd photoanode depends largely on the photogenerated holes. Generally, when a semiconductor is irradiated with light of appropriate energy, the photo excited electrons transfer from the valence band to the conduction band while holes occupy the valence band. However, the photogenerated electrons fall back within a short time to recombine with the photogenerated holes and this prevents the photogenerated holes from reacting with water molecules to produce hydroxyl radicals or directly oxidizing organic molecules present in the solution. In the case of CZnO-Pd photoanode, the efficiency of ZnO is greatly enhanced through improve charge carrier separation due to the presence of Pd. This is because when Pd is in contact with ZnO, a Schottky barrier is created which facilitated the migration of photogenerated holes from the conduction band of ZnO to Pd metal. Consequently, more photogenerated holes are readily available in the valence band of ZnO which either react directly with the paracetamol molecules or with water molecules to produce hydroxyl radicals which then oxidize the paracetamol to water and carbon dioxide. It is also important to note that electrons migrate from the photoanode to the cathode. These electrons could also produce superoxide radicals which can contribute to the degradation of the paracetamol molecules, however, the trapping experiments revealed that the contribution of superoxide radicals is negligible. There is also a possibility of the generation of hydrogen molecules on the cathode by the reactions of electrons with water molecules [100]. The proposed mechanism for the production of oxidants and degradation of paracetamol molecules is illustrated in the schematic diagram presented in Figure 7b (Mechanism PEC degradation process using CZnO-Pd100 photoanode).

.

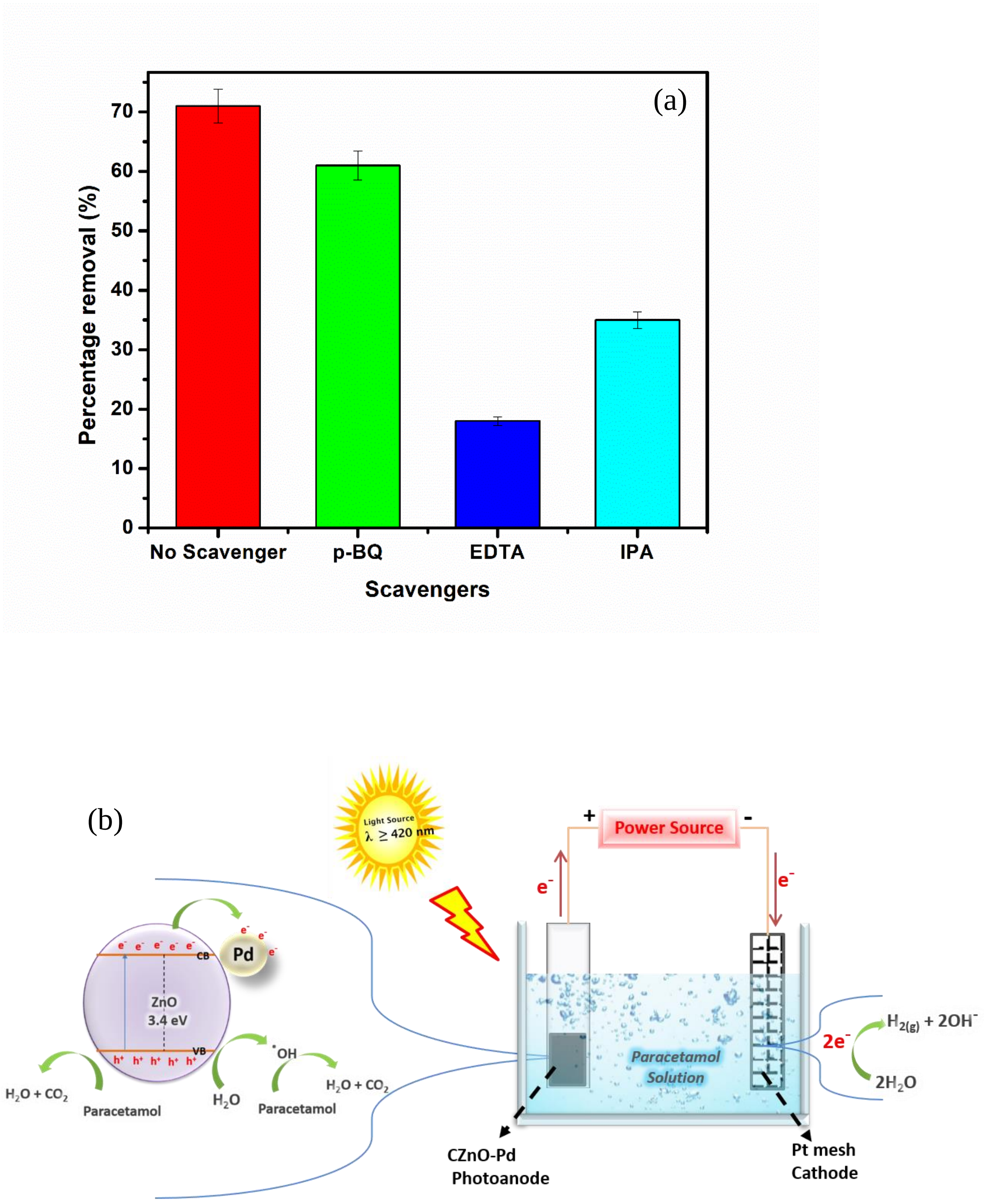

Figure 7: (a) PEC degradation of paracetamol in the presence on scavengers; (b) Mechanism PEC degradation process using CZnO-Pd100 photoanode (2 h; 0.1 mM paracetamol; 10 mA cm^{-2}; CZnO-Pd100)

3.2.3 Comparison with previous studies

Several kinds of semiconductor photoanodes have been explored for the PEC degradation of pharmaceuticals. To clearly justify the performance of the CZnO-Pd photoanode, the results obtained were compared with earlier literatures on PEC degradation of paracetamol. As presented in Table 1, the percentage removal as well as TOC removal obtained with the present electrode compares well with the previous studies and in fact, in some cases the electrode performed better than other earlier reported electrodes. Therefore, CZnO-Pd can be a suitable photoanode for the PEC removal of paracetamol molecules in wastewater.

Table 1: Comparison of electrode performance with previous studies

Photoanode	**Paracetamol concentration (mgL^{-1})**	**Percentage Removal**	**%TOC removal**	**References**
Au-TiO_2	78.5	66% after 3 h	20% after 3 h	[101]
TiO_2	60	100% after 70 min	-	[102]
$BiVO_4$/BiOI	10	68% after 2 h	59% after 2 h	[103]
TiO_2	40	45% after 4 h	21% after 4 h	[104]
CZnO-Pd	151	100% after 150 min	71% after 4 h	Present study

Conclusion

In this work, successful preparation of Pd loaded zinc oxide carbon nanofibers (CZnO-Pd) was achieved through electrospinning and atomic layer deposition. Results from the structural and morphological characterization revealed that amorphous ZnO nanoparticles were homogenously deposited on the surface of the carbon nanofibers while spherical metallic Pd nanoparticles were deposited on the edge/shell of the nanofibers to form a coaxial or core/shell structure. The prepared material (CZnO-Pd100) displayed good absorbance of photons in the visible light region due to the presence of metallic Pd. However, the visible light absorption of the material decreased with high content of Pd nanoparticles (ZCnO-Pd200). Similar trend was observed when the prepared materials were applied for the photoelectrocatalytic removal of paracetamol. Total removal was achieved in less than 3 h with 71.20 ± 0.31% TOC removal after 4 h with the use of CZnO-Pd100 while the percentage removal obtained with CZnO-Pd200 was lower due higher content of Pd particles which decreased the photocatalytic active of the semiconductor. Additionally, the rate of the PEC degradation process of paracetamol using the CZnO-Pd100 photoanode was fast and the mechanism of the reaction suggests that both photogenerated holes and hydroxyl radicals played substantial role in the degradation of the paracetamol molecules. Overall, the CZnO-Pd material has a great potential as photoanode for the mineralization of organic pollutants in wastewater.

Acknowledgments

E.C acknowledges the partial financial support from the National Science Centre (NCN) of Poland by the OPUS grant 2019/35/B/ST5/00248. O.A.A. acknowledges the National Research Foundation, South Africa (CPRR Grant number: 118546); Water Research Commission South Africa (Grant Number: K5/2567); Centre for Nanomaterials Science Research, University of Johannesburg; Faculty of Science, University of Johannesburg; Global Excellence and Stature (GES) doctoral support, University of Johannesburg; B. O. O. is grateful to University of Ilorin, Nigeria for study leave.

References

[1] C. Wu, C. Maurer, Y. Wang, S. Xue, D.L. Davis, Water pollution and human health in China, Environ. Health Perspect. 107 (1999) 251–256. doi:10.1289/ehp.99107251.

[2] A.S. Morshedy, H.R. Ali, A.A. Nada, A.M. Rabie, H.H. El-Maghrabi, Highly efficient Imprinted Polymer Nanocomposites for photocatalytic desulfurization of real diesel fuel, Environ. Technol. Innov. (2020). doi:10.1016/j.eti.2020.101206.

[3] A.A. Nada, H.R. Tantawy, M.A. Elsayed, M. Bechelany, M.E. Elmowafy, Elaboration of nano titania-magnetic reduced graphene oxide for degradation of tartrazine dye in aqueous solution, Solid State Sci. 78 (2018). doi:10.1016/j.solidstatesciences.2018.02.014.

[4] R. Elshypany, H. Selim, K. Zakaria, A.H. Moustafa, S.A. Sadeek, S.I. Sharaa, P. Raynaud, A.A. Nada, Magnetic ZnO Crystal Nanoparticle Growth on Reduced Graphene Oxide for Enhanced Photocatalytic Performance under Visible Light Irradiation, (2021).

[5] H.H. El-Maghrabi, A.A. Al-Kahlawy, A.A. Nada, T. Zaki, Photocorrosion resistant Ag2CO3@Fe2O3/TiO2-NT nanocomposite for efficient visible light photocatalytic degradation activities, J. Hazard. Mater. (2018). doi:10.1016/j.jhazmat.2018.08.002.

[6] A.A. Nada, M.F. Bekheet, S. Roualdes, A. Gurlo, A. Ayral, Functionalization of MCM-41 with titanium oxynitride deposited via PECVD for enhanced removal of methylene blue, J. Mol. Liq. (2019). doi:10.1016/j.molliq.2018.10.154.

[7] A.L. Spongberg, J.D. Witter, Pharmaceutical compounds in the wastewater process stream in Northwest Ohio, Sci. Total Environ. 397 (2008) 148–157. doi:10.1016/j.scitotenv.2008.02.042.

[8] D.G.J. Larsson, C. De Pedro, N. Paxeus, Effluent from drug manufactures contains extremely high levels of pharmaceuticals, 148 (2007) 751–755. doi:10.1016/j.jhazmat.2007.07.008.

[9] H.H. El-Maghrabi, E.A. Nada, F.S. Soliman, Y.M. Moustafa, A.E.-S. Amin, One pot environmental friendly nanocomposite synthesis of novel TiO2-nanotubes on graphene sheets as effective photocatalyst, Egypt. J. Pet. 25 (2016) 575–584.

[10] J. Wilkinson, P.S. Hooda, J. Barker, S. Barton, J. Swinden, Occurrence, fate and transformation of emerging contaminants in water: An overarching review of the field, Environ. Pollut. 231 (2017) 954–970. doi:10.1016/j.envpol.2017.08.032.

[11] J. Fick, H. Söderström, R.H. Lindberg, C. Phan, M. Tysklind, D.G.J. Larsson, Contamination of Surface, Ground, and Drinking Water From Pharmaceutical Production, Environ. Toxicol. Chem. 28 (2009) 2522. doi:10.1897/09-073.1.

[12] S. Mompelat, B. Le Bot, O. Thomas, Occurrence and fate of pharmaceutical products and by-products, from resource to drinking water, Environ. Int. 35 (2009) 803–814. doi:10.1016/j.envint.2008.10.008.

[13] N. Serpone, Y.M. Artemev, V.K. Ryabchuk, A. V. Emeline, S. Horikoshi, Light-driven advanced oxidation processes in the disposal of emerging pharmaceutical contaminants in aqueous media: A brief review, Curr. Opin. Green Sustain. Chem. 6 (2017) 18–33. doi:10.1016/j.cogsc.2017.05.003.

[14] T.B. Devi, M. Ahmaruzzaman, Bio-inspired facile and green fabrication of Au@Ag@AgCl core–double shells nanoparticles and their potential applications for elimination of toxic emerging pollutants: A green and efficient approach for wastewater

treatment, Chem. Eng. J. 317 (2017) 726–741. doi:10.1016/j.cej.2017.02.082.

[15] N. Kemper, Veterinary antibiotics in the aquatic and terrestrial environment, Ecol. Indic. 8 (2008) 1–13. doi:10.1016/j.ecolind.2007.06.002.

[16] P. Välitalo, A. Kruglova, A. Mikola, R. Vahala, Toxicological impacts of antibiotics on aquatic micro-organisms: A mini-review, Int. J. Hyg. Environ. Health. 220 (2017) 558–569. doi:10.1016/j.ijheh.2017.02.003.

[17] A.M. Deegan, B. Shaik, K. Nolan, K. Urell, M. Oelgemöller, J. Tobin, A. Morrissey, Treatment options for wastewater effluents from pharmaceutical companies, Int. J. Environ. Sci. Technol. 8 (2011) 649–666. doi:10.1007/BF03326250.

[18] C. Trellu, B.P. Chaplin, C. Coetsier, R. Esmilaire, S. Cerneaux, C. Causserand, M. Cretin, Electro-oxidation of organic pollutants by reactive electrochemical membranes, Chemosphere. 208 (2018) 159–175. doi:10.1016/j.chemosphere.2018.05.026.

[19] M.A. Oturan, J.J. Aaron, Advanced oxidation processes in water/wastewater treatment: Principles and applications. A review, Crit. Rev. Environ. Sci. Technol. 44 (2014) 2577–2641. doi:10.1080/10643389.2013.829765.

[20] E. Brillas, I. Sirés, M.A. Oturan, Electro-fenton process and related electrochemical technologies based on fenton’s reaction chemistry, Chem. Rev. 109 (2009) 6570–6631. doi:10.1021/cr900136g.

[21] O. Monfort, G. Plesch, Bismuth vanadate-based semiconductor photocatalysts: a short critical review on the efficiency and the mechanism of photodegradation of organic pollutants, Environ. Sci. Pollut. Res. 25 (2018) 19362–19379. doi:10.1007/s11356-018-

2437-9.

[22] M. El Kateb, C. Trellu, A. Darwich, M. Rivallin, M. Bechelany, S. Nagarajan, S. Lacour, N. Bellakhal, G. Lesage, M. Héran, M. Cretin, Electrochemical advanced oxidation processes using novel electrode materials for mineralization and biodegradability enhancement of nanofiltration concentrate of landfill leachates, Water Res. 162 (2019) 446–455. doi:10.1016/j.watres.2019.07.005.

[23] S. Garcia-Segura, E. Brillas, Applied photoelectrocatalysis on the degradation of organic pollutants in wastewaters, J. Photochem. Photobiol. C Photochem. Rev. 31 (2017) 1–35. doi:10.1016/j.jphotochemrev.2017.01.005.

[24] A.A. Nada, M. Nasr, R. Viter, P. Miele, S. Roualdes, M. Bechelany, Mesoporous ZnFe2O4@TiO2 nanofibers prepared by electrospinning coupled to PECVD as highly performing photocatalytic materials, J. Phys. Chem. C. (2017). doi:10.1021/acs.jpcc.7b08567.

[25] M.G. Peleyeju, O.A. Arotiba, Recent trend in visible-light photoelectrocatalytic systems for degradation of organic contaminants in water/wastewater, Environ. Sci. Water Res. Technol. 4 (2018) 1389–1411. doi:10.1039/c8ew00276b.

[26] S. Kawrani, M. Boulos, M.F. Bekheet, R. Viter, A.A. Nada, W. Riedel, S. Roualdes, D. Cornu, M. Bechelany, Segregation of copper oxide on calcium copper titanate surface induced by Graphene Oxide for Water splitting applications, Appl. Surf. Sci. 516 (2020) 146051.

[27] S. Kawrani, A.A. Nada, M.F. Bekheet, M. Boulos, R. Viter, S. Roualdes, P. Miele, D. Cornu, M. Bechelany, Enhancement of calcium copper titanium oxide

photoelectrochemical performance using boron nitride nanosheets, Chem. Eng. J. 389 (2020). doi:10.1016/j.cej.2020.124326.

[28] O.A. Arotiba, B.O. Orimolade, B.A. Koiki, Visible Light Driven Photoelectrocatalytic Semiconductor Heterojunction Anodes for Water Treatment Applications, Curr. Opin. Electrochem. (2020) 1–10. doi:10.1016/j.coelec.2020.03.018.

[29] R. Daghrir, P. Drogui, D. Robert, Photoelectrocatalytic technologies for environmental applications, J. Photochem. Photobiol. A Chem. 238 (2012) 41–52. doi:10.1016/j.jphotochem.2012.04.009.

[30] A. Miquelot, L. Youssef, C. Villeneuve-Faure, N. Prud'Homme, N. Dragoe, A. Nada, V. Rouessac, S. Roualdes, J. Bassil, M. Zakhour, In-and out-plane transport properties of chemical vapor deposited TiO 2 anatase films, J. Mater. Sci. 56 (2021) 10458–10476.

[31] B.O. Orimolade, O.A. Arotiba, An Exfoliated Graphite-Bismuth Vanadate Composite Photoanode for the Photoelectrochemical Degradation of Acid Orange 7 Dye, Electrocatalysis. 10 (2019) 429–435. doi:10.1007/s12678-019-00534-5.

[32] Y. Zhou, X. Fan, G. Zhang, W. Dong, Fabricating MoS 2 nanoflakes photoanode with unprecedented high photoelectrochemical performance and multi-pollutants degradation test for water treatment, Chem. Eng. J. 356 (2019) 1003–1013. doi:10.1016/j.cej.2018.09.097.

[33] B.A. Koiki, B.O. Orimolade, B.N. Zwane, D. Nkosi, N. Mabuba, O.A. Arotiba, Cu2O on anodised TiO2 nanotube arrays: A heterojunction photoanode for visible light assisted electrochemical degradation of pharmaceuticals in water, Electrochim. Acta. 340 (2020) 135944. doi:10.1016/j.electacta.2020.135944.

[34] M. Zhang, W. Pu, S. Pan, O.K. Okoth, C. Yang, J. Zhang, Photoelectrocatalytic activity of liquid phase deposited α-Fe2O3 films under visible light illumination, J. Alloys Compd. 648 (2015) 719–725. doi:10.1016/j.jallcom.2015.07.026.

[35] E.H. Umukoro, M.G. Peleyeju, J.C. Ngila, O.A. Arotiba, Towards wastewater treatment: Photo-assisted electrochemical degradation of 2-nitrophenol and orange II dye at a tungsten trioxide-exfoliated graphite composite electrode, Chem. Eng. J. 317 (2017) 290–301. doi:10.1016/j.cej.2017.02.084.

[36] M. Pirhashemi, A. Habibi-Yangjeh, S. Rahim Pouran, Review on the criteria anticipated for the fabrication of highly efficient ZnO-based visible-light-driven photocatalysts, J. Ind. Eng. Chem. 62 (2018) 1–25. doi:10.1016/j.jiec.2018.01.012.

[37] A.J. de Walle, C.G. Van, Fundamentals of zinc oxide as a semiconductor, Reports Prog. Phys. 72 (2009) 126501.

[38] A.B. Djurišić, X. Chen, Y.H. Leung, A. Man Ching Ng, ZnO nanostructures: Growth, properties and applications, J. Mater. Chem. 22 (2012) 6526–6535. doi:10.1039/c2jm15548f.

[39] H. Wang, S. Cao, B. Yang, H. Li, M. Wang, X. Hu, K. Sun, Z. Zang, NH 4 Cl-Modified ZnO for High-Performance CsPbIBr 2 Perovskite Solar Cells via Low-Temperature Process, Sol. RRL. 4 (2020) 1900363. doi:10.1002/solr.201900363.

[40] H. Wang, P. Zhang, Z. Zang, High performance CsPbBr3 quantum dots photodetectors by using zinc oxide nanorods arrays as an electron-transport layer, Appl. Phys. Lett. 116 (2020) 162103. doi:10.1063/5.0005464.

[41] J.S. Yang, J.J. Wu, Low-potential driven fully-depleted BiVO4/ZnO heterojunction nanodendrite array photoanodes for photoelectrochemical water splitting, Nano Energy. 32 (2017) 232–240. doi:10.1016/j.nanoen.2016.12.039.

[42] W. Chen, W. Wu, W. Yang, J. Zhao, M. Xiao, W. Kong, CdCl2-assisting heat-treatment: Enhanced photoelectrocatalytic hydrogen generation and stability of CdS/ZnO nanoheterojunction arrays, Int. J. Hydrogen Energy. 43 (2018) 9969–9977. doi:10.1016/j.ijhydene.2018.04.045.

[43] T.N. Trung, D.B. Seo, N.D. Quang, D. Kim, E.T. Kim, Enhanced photoelectrochemical activity in the heterostructure of vertically aligned few-layer MoS2 flakes on ZnO, Electrochim. Acta. 260 (2018) 150–156. doi:10.1016/j.electacta.2017.11.089.

[44] A.P.P. da Rosa, R.P. Cavalcante, T.F. da Silva, F. Gozzi, C. Byrne, E. McGlynn, G.A. Casagrande, S.C. de Oliveira, A.M. Junior, Photoelectrocatalytic Degradation of Methylene Blue Using ZnO Nanorods Fabricated on Silicon Substrates, J. Nanosci. Nanotechnol. 20 (2019) 1177–1188. doi:10.1166/jnn.2020.16961.

[45] M. Hosseini, A. Esrafili, M. Farzadkia, M. Kermani, M. Gholami, Degradation of ciprofloxacin antibiotic using photo-electrocatalyst process of Ni-doped ZnO deposited by RF sputtering on FTO as an anode electrode from aquatic environments: Synthesis, kinetics, and ecotoxicity study, Microchem. J. 154 (2020) 104663. doi:10.1016/j.microc.2020.104663.

[46] J. Feng, Y. Tian, O.K. Okoth, L. Cheng, J. Zhang, Liquid Phase Deposition of Nickel-Doped ZnO Film with Enhanced Visible Light Photoelectrocatalytic Activity, J. Electrochem. Soc. 166 (2019) H685–H690. doi:10.1149/2.0361914jes.

[47] W. Fei, H. Li, N. Li, D. Chen, Q. Xu, H. Li, J. He, J. Lu, Facile fabrication of ZnO/MoS2 p-n junctions on Ni foam for efficient degradation of organic pollutants through photoelectrocatalytic process, Sol. Energy. 199 (2020) 164–172. doi:10.1016/j.solener.2020.02.037.

[48] J. Feng, L. Cheng, J. Zhang, O.K. Okoth, F. Chen, Preparation of BiVO4/ZnO composite film with enhanced visible-light photoelectrocatalytic activity, Ceram. Int. 44 (2018) 3672–3677. doi:10.1016/j.ceramint.2017.11.124.

[49] B.O. Orimolade, B.A. Koiki, B.N. Zwane, G.M. Peleyeju, N. Mabuba, O.A. Arotiba, Interrogating solar photoelectrocatalysis on an exfoliated graphite–BiVO $_4$ /ZnO composite electrode towards water treatment, RSC Adv. 9 (2019) 16586–16595. doi:10.1039/C9RA02366F.

[50] J. Wang, H. Zhu, J.D. Chen, B. Zhang, M. Zhang, L.N. Wang, M.L. Du, Small and well-dispersed Cu nanoparticles on carbon nanofibers: Self-supported electrode materials for efficient hydrogen evolution reaction, Int. J. Hydrogen Energy. 41 (2016) 18044–18049. doi:10.1016/j.ijhydene.2016.08.058.

[51] J. Wang, H. Zhu, D. Yu, J.W. Chen, J.D. Chen, M. Zhang, L.N. Wang, M.L. Du, Engineering the Composition and Structure of Bimetallic Au-Cu Alloy Nanoparticles in Carbon Nanofibers: Self-Supported Electrode Materials for Electrocatalytic Water Splitting, ACS Appl. Mater. Interfaces. 9 (2017) 19756–19765. doi:10.1021/acsami.7b01418.

[52] M. Najem, A.A. Nada, M. Weber, S. Sayegh, A. Razzouk, C. Salameh, C. Eid, M. Bechelany, Palladium/Carbon Nanofibers by Combining Atomic Layer Deposition and

Electrospinning for Organic Pollutant Degradation, Materials (Basel). 13 (2020) 1947.

[53] C. Zhou, C. Lai, D. Huang, G. Zeng, C. Zhang, Highly porous carbon nitride by supramolecular preassembly of monomers for photocatalytic removal of sulfamethazine under visible light driven, Appl. Catal. B Environ. 220 (2018) 202–210. doi:10.1016/j.apcatb.2017.08.055.

[54] A. Barhoum, H.H. El-Maghrabi, I. Iatsunskyi, E. Coy, A. Renard, C. Salameh, M. Weber, S. Sayegh, A.A. Nada, S. Roualdes, M. Bechelany, Atomic layer deposition of Pd nanoparticles on self-supported carbon-Ni/NiO-Pd nanofiber electrodes for electrochemical hydrogen and oxygen evolution reactions, J. Colloid Interface Sci. 569 (2020) 286–297. doi:10.1016/j.jcis.2020.02.063.

[55] H.H. El-Maghrabi, A.A. Nada, S. Roualdes, M.F. Bekheet, Design of Ni/NiO–TiO2/rGO nanocomposites on carbon cloth conductors via PECVD for electrocatalytic water splitting, Int. J. Hydrogen Energy. 45 (2020) 32000–32011.

[56] T. Cai, Y. Huang, M. Huang, Y. Xi, D. Pang, W. Zhang, Enhancing oxygen reduction reaction of supercapacitor microbial fuel cells with electrospun carbon nanofibers composite cathode, Chem. Eng. J. 371 (2019) 544–553. doi:10.1016/j.cej.2019.04.025.

[57] Q. Ding, M. Liu, Y.-E. Miao, Y. Huang, T. Liu, Electrospun nickel-decorated carbon nanofiber membranes as efficient electrocatalysts for hydrogen evolution reaction, Electrochim. Acta. 159 (2015) 1–7. doi:10.1016/J.ELECTACTA.2015.01.197.

[58] M. El-Sayed, A.A. Nada, Polyethylenimine −functionalized amorphous carbon fabricated from oil palm leaves as a novel adsorbent for Cr(VI) and Pb(II) from aqueous solution, J. Water Process Eng. (2017). doi:10.1016/j.jwpe.2017.02.012.

[59] A.A. Nada, M.F. Bekheet, R. Viter, P. Miele, S. Roualdes, M. Bechelany, BN/GdxTi (1-x) O (4-x)/2 nanofibers for enhanced photocatalytic hydrogen production under visible light, Appl. Catal. B Environ. 251 (2019) 76–86. doi:10.1016/j.apcatb.2019.03.043.

[60] H.H. El-Maghrabi, A.A. Nada, M.F. Bekheet, S. Roualdes, W. Riedel, I. Iatsunskyi, E. Coy, A. Gurlo, M. Bechelany, Coaxial nanofibers of nickel/gadolinium oxide/nickel oxide as highly effective electrocatalysts for hydrogen evolution reaction, J. Colloid Interface Sci. (2020). doi:https://doi.org/10.1016/j.jcis.2020.11.103.

[61] M. Weber, A. Julbe, A. Ayral, P. Miele, M. Bechelany, Atomic Layer Deposition for Membranes: Basics, Challenges, and Opportunities, Chem. Mater. 30 (2018) 7368–7390. doi:10.1021/acs.chemmater.8b02687.

[62] O. Graniel, M. Weber, S. Balme, P. Miele, M. Bechelany, Atomic layer deposition for biosensing applications, Biosens. Bioelectron. 122 (2018) 147–159. doi:10.1016/j.bios.2018.09.038.

[63] M. Weber, N. Tuleushova, J. Zgheib, C. Lamboux, I. Iatsunskyi, E. Coy, V. Flaud, S. Tingry, D. Cornu, P. Miele, Enhanced electrocatalytic performance triggered by atomically bridged boron nitride between palladium nanoparticles and carbon fibers in gas-diffusion electrodes, Appl. Catal. B Environ. 257 (2019) 117917.

[64] E.J. Ruiz, A. Hernández-Ramírez, J.M. Peralta-Hernández, C. Arias, E. Brillas, Application of solar photoelectro-Fenton technology to azo dyes mineralization: Effect of current density, Fe2+ and dye concentrations, Chem. Eng. J. 171 (2011) 385–392. doi:10.1016/j.cej.2011.03.004.

[65] T.X. Huong Le, L.F. Dumée, S. Lacour, M. Rivallin, Z. Yi, L. Kong, M. Bechelany, M.

Cretin, Hybrid graphene-decorated metal hollow fibre membrane reactors for efficient electro-Fenton - Filtration co-processes, J. Memb. Sci. 587 (2019) 117182. doi:10.1016/j.memsci.2019.117182.

[66] N. Soltani, U. Simon, A. Bahrami, X. Wang, S. Selve, J.D. Epping, M.I. Pech-Canul, M.F. Bekheet, A. Gurlo, Macroporous polymer-derived SiO2/SiOC monoliths freeze-cast from polysiloxane and amorphous silica derived from rice husk, J. Eur. Ceram. Soc. 37 (2017) 4809–4820.

[67] H. Takagi, K. Maruyama, N. Yoshizawa, Y. Yamada, Y. Sato, XRD analysis of carbon stacking structure in coal during heat treatment, Fuel. 83 (2004) 2427–2433.

[68] H.H. El-Maghrabi, S.M. Abdelmaged, A.A. Nada, F. Zahran, S.A. El-Wahab, D. Yahea, G.M. Hussein, M.S. Atrees, Magnetic graphene based nanocomposite for uranium scavenging, J. Hazard. Mater. 322 (2017). doi:10.1016/j.jhazmat.2016.10.007.

[69] A. Baylet, P. Marecot, D. Duprez, P. Castellazzi, G. Groppi, P. Forzatti, In situ Raman and in situ XRD analysis of PdO reduction and Pd oxidation supported on γ-Al 2 O 3 catalyst under different atmospheres, Phys. Chem. Chem. Phys. 13 (2011) 4607–4613.

[70] H. Sun, Y. Zhu, B. Yang, Y. Wang, Y. Wu, J. Du, Template-free fabrication of nitrogen-doped hollow carbon spheres for high-performance supercapacitors based on a scalable homopolymer vesicle, J. Mater. Chem. A. 4 (2016) 12088–12097.

[71] J. Wang, V. Schölch, O. Görke, G. Schuck, X. Wang, G. Shao, S. Schorr, M.F. Bekheet, A. Gurlo, Metal-containing ceramic nanocomposites synthesized from metal acetates and polysilazane, Open Ceram. (2020) 100001.

[72] M. Nasr, R. Viter, C. Eid, F. Warmont, R. Habchi, P. Miele, M. Bechelany, Synthesis of novel ZnO/ZnAl 2 O 4 multi co-centric nanotubes and their long-term stability in photocatalytic application, RSC Adv. 6 (2016) 103692–103699.

[73] B.K. Gupta, V. Shanker, M. Arora, D. Haranath, Photoluminescence and electron paramagnetic resonance studies of springlike carbon nanofibers, Appl. Phys. Lett. 95 (2009) 73115.

[74] T. Dexin, W. Yanli, G. Ying, Facile Visible-Light-Assisted Synthesis, Optical, and Electrochemical Properties of Pd Nanoparticles with Single-crystalline and Multiple-twinned Structures, Rare Met. Mater. Eng. 46 (2017) 2065–2069. doi:https://doi.org/10.1016/S1875-5372(17)30180-7.

[75] C.-L. Lee, C.-M. Tseng, R.-B. Wu, C.-C. Wu, S.-C. Syu, Catalytic characterization of hollow silver/palladium nanoparticles synthesized by a displacement reaction, Electrochim. Acta. 54 (2009) 5544–5547. doi:https://doi.org/10.1016/j.electacta.2009.04.056.

[76] B.P. Narasaiah, B.K. Mandal, Remediation of azo-dyes based toxicity by agro-waste cotton boll peels mediated palladium nanoparticles, J. Saudi Chem. Soc. 24 (2020) 267–281. doi:https://doi.org/10.1016/j.jscs.2019.11.003.

[77] X. Lu, M. Rycenga, S.E. Skrabalak, B. Wiley, Y. Xia, Chemical Synthesis of Novel Plasmonic Nanoparticles, Annu. Rev. Phys. Chem. 60 (2009) 167–192. doi:10.1146/annurev.physchem.040808.090434.

[78] K.H. Leong, H.Y. Chu, S. Ibrahim, P. Saravanan, Palladium nanoparticles anchored to anatase TiO2 for enhanced surface plasmon resonance-stimulated, visible-light-driven

photocatalytic activity, Beilstein J. Nanotechnol. 6 (2015) 428–437. doi:10.3762/bjnano.6.43.

[79] J.-H. Kim, A. Mirzaei, H.W. Kim, S.S. Kim, Pd functionalization on ZnO nanowires for enhanced sensitivity and selectivity to hydrogen gas, Sensors Actuators B Chem. 297 (2019) 126693.

[80] C. Cseko, Z. Bagi, A. Koller, Biphasic effect of hydrogen peroxide on skeletal muscle arteriolar tone via activation of endothelial and smooth muscle signaling pathways, J. Appl. Physiol. 97 (2004) 1130–1137.

[81] Y. Zhang, Q. Wang, J. Xu, S. Ma, Synthesis of Pd/ZnO nanocomposites with high photocatalytic performance by a solvothermal method, Appl. Surf. Sci. 258 (2012) 10104–10109.

[82] A. Merenda, M. Weber, M. Bechelany, F.-M. Allioux, L. Hyde, L. Kong, L.F. Dumée, Fabrication of Pd-TiO2 nanotube photoactive junctions via Atomic Layer Deposition for persistent pesticide pollutants degradation, Appl. Surf. Sci. 483 (2019) 219–230.

[83] T. Chen, S. Yu, X. Fang, H. Huang, L. Li, X. Wang, H. Wang, Enhanced photocatalytic activity of C@ZnO core-shell nanostructures and its photoluminescence property, Appl. Surf. Sci. 389 (2016) 303–310. doi:10.1016/j.apsusc.2016.07.122.

[84] Y. Chang, J. Xu, Y. Zhang, S. Ma, L. Xin, L. Zhu, C. Xu, Optical properties and photocatalytic performances of Pd modified ZnO samples, J. Phys. Chem. C. 113 (2009) 18761–18767. doi:10.1021/jp9050808.

[85] Y.C. Liang, W.K. Liao, X.S. Deng, Synthesis and substantially enhanced gas sensing

sensitivity of homogeneously nanoscale Pd- and Au-particle decorated ZnO nanostructures, J. Alloys Compd. 599 (2014) 87–92. doi:10.1016/j.jallcom.2014.01.167.

[86] V. Nguyen, J. Si, L. Yan, X. Hou, Electron-hole recombination dynamics in carbon nanodots, Carbon N. Y. 95 (2015) 659–663. doi:10.1016/j.carbon.2015.08.066.

[87] V. Nguyen, J. Si, L. Yan, X. Hou, Direct demonstration of photoluminescence originated from surface functional groups in carbon nanodots, Carbon N. Y. 108 (2016) 268–273. doi:10.1016/j.carbon.2016.07.019.

[88] P. Erhart, K. Albe, A. Klein, First-principles study of intrinsic point defects in ZnO: Role of band structure, volume relaxation, and finite-size effects, Phys. Rev. B. 73 (2006) 205203.

[89] I. Iatsunskyi, G. Gottardi, V. Micheli, R. Canteri, E. Coy, M. Bechelany, Atomic layer deposition of palladium coated TiO2/Si nanopillars: ToF-SIMS, AES and XPS characterization study, Appl. Surf. Sci. 542 (2021) 148603.

[90] Y. Xie, P.M.A. Sherwood, X-ray photoelectron-spectroscopic studies of carbon fiber surfaces. Part 13. Valence-band studies of oxidized fibers interpreted by X. alpha. calculations, Chem. Mater. 3 (1991) 164–168.

[91] A. Barhoum, H.H. El-Maghrabi, A.A. Nada, S. Sayegh, A. Renard, I. Iatsunskyi, E. Coy, M. Bechelany, Simultaneous Hydrogen and Oxygen Evolution Reactions using Free-Standing Nitrogen-Doped-Carbon-Co/CoOx Nanofiber Electrodes Decorated with Palladium Nanoparticles, J. Mater. Chem. A. (2021).

[92] J.B. Zhong, J.Z. Li, X.Y. He, J. Zeng, Y. Lu, W. Hu, K. Lin, Improved photocatalytic

performance of Pd-doped ZnO, Curr. Appl. Phys. 12 (2012) 998–1001. doi:10.1016/j.cap.2012.01.003.

[93] F.S. Hashim, A.F. Alkaim, S.J. Salim, A.H.O. Alkhayatt, Effect of (Ag, Pd) doping on structural, and optical properties of ZnO nanoparticales: As a model of photocatalytic activity for water pollution treatment, Chem. Phys. Lett. 737 (2019) 136828. doi:10.1016/j.cplett.2019.136828.

[94] V.M. Daskalaki, I. Fulgione, Z. Frontistis, L. Rizzo, D. Mantzavinos, Solar light-induced photoelectrocatalytic degradation of bisphenol-A on TiO2/ITO film anode and BDD cathode, Catal. Today. 209 (2013) 74–78. doi:10.1016/j.cattod.2012.07.026.

[95] Z. Frontistis, V.M. Daskalaki, A. Katsaounis, I. Poulios, D. Mantzavinos, Electrochemical enhancement of solar photocatalysis: Degradation of endocrine disruptor bisphenol-A on Ti/TiO2 films, Water Res. 45 (2011) 2996–3004. doi:10.1016/j.watres.2011.03.030.

[96] T.X.H. Le, T. Van Nguyen, Z. Amadou Yacouba, L. Zoungrana, F. Avril, D.L. Nguyen, E. Petit, J. Mendret, V. Bonniol, M. Bechelany, S. Lacour, G. Lesage, M. Cretin, Correlation between degradation pathway and toxicity of acetaminophen and its by-products by using the electro-Fenton process in aqueous media, Chemosphere. 172 (2017) 1–9. doi:10.1016/j.chemosphere.2016.12.060.

[97] H. Olvera-Vargas, J.C. Rouch, C. Coetsier, M. Cretin, C. Causserand, Dynamic cross-flow electro-Fenton process coupled to anodic oxidation for wastewater treatment: Application to the degradation of acetaminophen, Sep. Purif. Technol. 203 (2018) 143–151. doi:10.1016/j.seppur.2018.03.063.

[98] S.O. Ganiyu, N. Oturan, S. Raffy, G. Esposito, E.D. van Hullebusch, M. Cretin, M.A.

Oturan, Use of Sub-stoichiometric Titanium Oxide as a Ceramic Electrode in Anodic Oxidation and Electro-Fenton Degradation of the Beta-blocker Propranolol: Degradation Kinetics and Mineralization Pathway, Electrochim. Acta. 242 (2017) 344–354. doi:10.1016/j.electacta.2017.05.047.

[99] M.A. Oturan, M. Pimentel, N. Oturan, I. Sirés, Reaction sequence for the mineralization of the short-chain carboxylic acids usually formed upon cleavage of aromatics during electrochemical Fenton treatment, Electrochim. Acta. 54 (2008) 173–182. doi:10.1016/j.electacta.2008.08.012.

[100] P.J. Espinoza-Montero, C. Vega-Verduga, P. Alulema-Pullupaxi, L. Fernández, J.L. Paz, Technologies Employed in the Treatment of Water Contaminated with Glyphosate: A Review, Molecules. 25 (2020) 5550. doi:10.3390/molecules25235550.

[101] R. Hernández, I. Olvera-Rodríguez, C. Guzmán, A. Medel, L. Escobar-Alarcón, E. Brillas, I. Sirés, K. Esquivel, Microwave-assisted sol-gel synthesis of an Au-TiO2 photoanode for the advanced oxidation of paracetamol as model pharmaceutical pollutant, Electrochem. Commun. 96 (2018) 42–46. doi:10.1016/j.elecom.2018.09.009.

[102] R. Katal, M.H. Davood Abadi Farahani, H. Jiangyong, Degradation of acetaminophen in a photocatalytic (batch and continuous system) and photoelectrocatalytic process by application of faceted-TiO2, Sep. Purif. Technol. 230 (2020) 115859. doi:10.1016/j.seppur.2019.115859.

[103] B.O. Orimolade, B.A. Koiki, G.M. Peleyeju, O.A. Arotiba, Visible light driven photoelectrocatalysis on a FTO/BiVO 4 /BiOI anode for water treatment involving emerging pharmaceutical pollutants, Electrochim. Acta. 307 (2019) 285–292.

doi:10.1016/j.electacta.2019.03.217.

[104] J. Borràs-Ferrís, R. Sánchez-Tovar, E. Blasco-Tamarit, M.J. Muñoz-Portero, R.M. Fernández-Domene, J. García-Antón, TiO 2 nanostructures for photoelectrocatalytic degradation of acetaminophen, Nanomaterials. 9 (2019) 1–13. doi:10.3390/nano9040583.